

A Generalized Constitutive Framework for the Kinematics and Kinetics of In-Parallel-Actuated Soft Robot Manipulators

Olalekan Ogunmolu

The University of Pennsylvania, Philadelphia, PA 19104, USA.

Olalekan.Ogunmolu@pennmedicine.upenn.edu,

<http://scriptedonachip.com>

Abstract. The kinematics and dynamics of a parallel soft multi-degree of freedom robot is here put forward to counterbalance the preoccupation with rigid robot mechanisms today. Rigid robots in open kinematic arrangements have high load-to-weight ratios and the flexure of their links limit their use in precision manipulation tasks. Their parallel counterparts are often unsafe in medical robotics owing to their high-tensile components. These prompt our study of the kinematics and kinetics of soft mechanisms using ideas from continuum mechanics and differential geometry. We then derive the Newton-Euler system of equations for the kinetics using elasticity theory. Relating the solutions to the boundary value problem of the Cauchy stress for the soft robots to the wrenches on an object or load, we write out the manipulation map and construct the associated Jacobian for its direct positioning analysis. Within the bounds here set, the fully-actuated provide the full range of motion manipulation in six dimensions. Our goal is to edge open the door a little further towards in-parallel soft actuation mechanisms that are cheaper, medically useful, lightweight and modular for precision manipulation tasks today.

Keywords: continuum mechanics, finite elastic deformations, differential geometry, soft robotics

We first present the type and number syntheses of the possible mechanisms that produce a 6-DOF end-effector motion in a tool frame

and underactuated mechanisms

1 Introduction

As automation evolves in factories, medical clinics, and business value chains, the limitations of rigid robots is becoming clearer for all to see namely, their low transportable loads, large flexure torques, and energy inefficiency. This is particularly all-the-more apparent in the pervasive open kinematic chains that are most prevalent in manipulation nowadays. For sophisticated control or motion manipulation tasks, these robots possess an uncanny difficulty in terms of safe motion planning. This is mostly due to their large weights which are derived from the stiffness of their rigid links – so designed to overcome the large flexure of torques at the joints. As such, there has been steady and growing interest in using soft robots to replace traditional automation tasks that rigid robots have otherwise found use [6, 20, 35]. Their design, often inspired from nature or biomimicry, leverages morphological computation that allows them to grasp objects in ways that rigid robots cannot [25, 40]. Whereas the freedom of rigid robots

are controlled by actuators with specific degrees of freedom, building specific degrees of freedom (DOF) into a soft robot is a concerted task that requires rethinking the manufacturing process of their (e.g. rubber or silicone) components [26], [27], since soft robots typically exhibit many to infinite degrees of freedom in their deformation state [31], [21]. As such the kinematics and dynamics of mechanisms constituted out of soft linkages need a new thinking approach when designing and assembling linkages made out of soft systems [24], [23].

We propose a finite elastic deformation model [16, 19, 33], based on the deformation invariants of the stored energy function for our soft robots, henceforth called inflatable air bladders or IABs. In what follows, we briefly describe our motivation for devising a finite elastic deformation model. The constant curvature approach for parameterizing the deformation of continuum robots [8, 9, 12] has played a significant role in the kinematic synthesis of deformable continuum models over the past three decades. Under this framework, the configuration space of a soft robot (SoRo) module is parameterized by the curvature of an arc projected on the SoRo's body, the arc's length, and the angle subtended by a tangent along that arc. The relationship between these parameters are typically found using differential kinematics with a Frenet-Serret frame that models a curve on the SoRo's surface – with or without torsion.

By abstracting an infinite dimensional structure to 3D, large portions of the manipulator dynamics are discarded under the assumption that the actuator design is symmetric and uniform in shape. This makes the constant curvature model overly simplistic so that it often exhibits poor performance in position control [13]. While the Cosserat brothers' beam theory has been relatively successful in modeling soft continuum dynamics [29, 34], its complexity, and sensing cost does not justify the alternatives [6].

Contributions: We present parallel multi-degree of freedom soft robotic systems made out of deformable spherical shells. The individual spherical shells are constrained to strain along specific directions in spherical coordinates and their kinematic arrangement have specially designed connectivity criterions [11] whose actuation freedoms [11] are constrained to yield the desired range of motions for the complete manipulation of an object located in their workspace along all possible range of motions (based on the Cartesian coordinates and Fick angles).

- We first provide a constitutive model that governs their deformation given the baked deformation constraints into the material properties of the robots
- We present the type-synthesis of the possible configurations of these soft parallel systems necessary to achieve the full range of motion manipulation of an object in six dimensions
- We analyze the manipulability measure and manipulability ellipsoid for these possible configurations
- We analyze the number- and size- synthesis of the various mechanisms that are achievable with our soft actuation systems
- Lastly, we analyze the kinematics and kinetics of the mechanism with the minimal number of linkages that achieves 6-DOF manipulability.

The common notations throughout the rest of this article are as defined in [Table 1](#).

Table 1. Common Notations in Article

Notation	Definition	Notation	Definition
B	An open set of particles on a Body, B	\mathcal{B}_o	Closure of the B in a reference configuration χ_0 over which a non-negative measure of mass is defined.
$\chi(X)$	The motion of particles X in \mathcal{B} . χ is an invertible C^2 diffeomorphism.	$\chi^{-1}(\mathbf{x})$	A region occupied by \mathbf{x} (the Euclidean equivalent of X) in configuration χ .
\mathbf{F}	The deformation gradient tensor, $\mathbf{F} = \nabla \chi_k(\mathbf{X}) = \dot{\chi}_k(\mathbf{X})$.	$\boldsymbol{\sigma}$	The Cauchy stress tensor.
\mathbf{C}	The right Cauchy-Green Tensor, $\mathbf{C} = \mathbf{F}^T \mathbf{F}$.	\mathbf{B}	The left Cauchy-Green Tensor, $\mathbf{B} = \mathbf{F} \mathbf{F}^T$.
$\mathbf{v}(\mathbf{x})$	The velocity field $\dot{\chi}(\mathbf{x})$	$\mathbf{a}(\mathbf{x})$	The acceleration field $\ddot{\chi}(\mathbf{x}) = \dot{\mathbf{v}}(\mathbf{x})$.

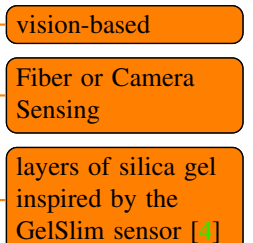
2 Mechanisms Description

2.1 Single Soft Robot Mechanism

Inspired by the papillae of cephalopods (such as octopus and cuttlefish) with respect to their ability to change their perfectly planar and smooth physical texture into a 3D texture up to a specific maximum size [1], we model our soft robots similar to the papillae of these organisms. Here, the elasticity of the soft robot is controlled by a muscular hydrostatic mechanism whereby an elastomeric dermis antagonizes the muscle fibers – causing uniaxial shape erection. We construct the elastic membranes of these soft robots from elastomeric rubber with a shore hardness of 10A (Dragon Skin 10-Medium, Smooth-on Inc.) and control the circumferential strain with nonwoven fabric meshes (Fleishman Fabrics & Supplies, Philadelphia, PA) similar to the design of [27, 28]. Furthermore, inspired by the innervated fins of cuttlefish which allow their mechanoreceptors to process tactile information from their immediate surroundings, we integrate tactile sensorson the outer walls of our soft robots to gather cues for required specific deformations [7]. For this layer, we embed .

This internal cavity contributes a single degree of freedom to a soft actuator linkage in the system – in part holding the object in place and moving the it as needed. Each IAB in the closed kinematic chain is linked to the object – each supporting only a part of the total load, redistributing link-loads and solving some of the problems with serial links. Figures 2 - 3 depict the structural characterization of the soft robot mechanism. Inspired by [27], the soft robot chambers are constrained to deform only along the radial strain in order to exert appropriate push on an object.

The robots are planar-shaped with a wall thickness of 1cm and diameter of 9cm.



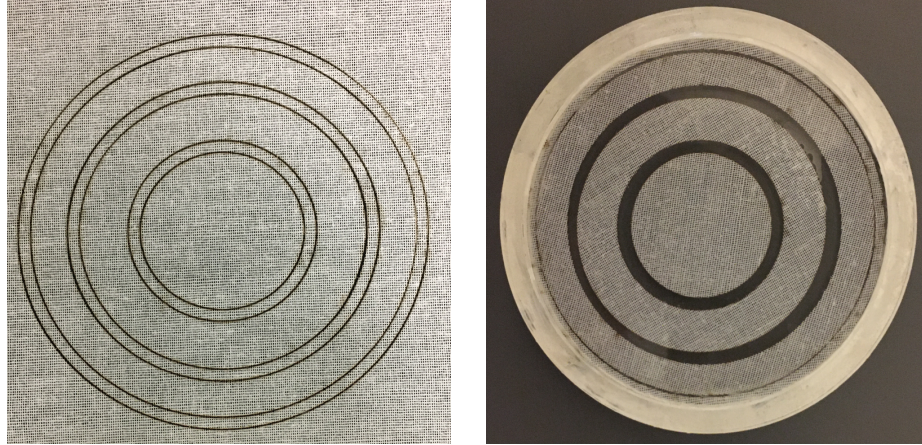


Fig. 1. Fabrication of the soft robot. **Left:** A non-woven fabric is laser-cut in concentric circular patterns. **Right:** Uncured silicone (Equal parts of Dragon Skin 10 Medium A and B) with the fabric membrane laid on it (the cuts have been removed). The admixture is allowed to cure at room temperature before demolding. We further post-cured the admixture at $176^{\circ}F$ for 2 hours and $212^{\circ}F$ for 1 hour respectively in order to allow the rubber material to attain its maximum physical properties.

2.2 Mechanisms Setup

We now describe the mechanism of the complete motion compensation system. We propose 3 IAB kinematic chains totaling 8 IABs around the patient's H&N region as illustrated in [Figure 5](#). The IABs have an internal cavity surrounded by two shells, which are made out of incompressible rubber materials with a Poisson's ratio of approximately 0.5. For simulation purposes, the internal shell has a wall thickness of 2.5cm.

The internal cavity ensures the hollow IAB holds the head in place. The outer shell encapsulates the inner shell such that local volume preservation is fulfilled between configuration changes. This isochoric property and the incompressibility constraints of the IAB material is important in the mathematical derivations of the mechanism's constitutive model. Each IAB in the closed kinematic chain is linked to the couch – each supporting only a part of the total load, redistributing link-loads and solving some of the problems with serial links. It would like to have the contacting regions between the IABs and head and neck locations to have regions of their surfaces shaped into profiles that allow continuous contact along e.g. a curve or a straight line. This would enforce nonholonomic constraints as the bodies roll without slipping at the *region of contact* on one another. This way, the load that an IAB supports would be distributed over a narrow strip, essentially an atlas, rather than a localized region around a point. An engaging pair of 3D-printed teeth on spur gears would touch along a straight line; helical, hypoid or worm gears would have engaging teeth along complicated spatial curves that enforce this constraint. This constraint is important since it would allow us define the profile of the motion when the IAB exerts a motion on the head.

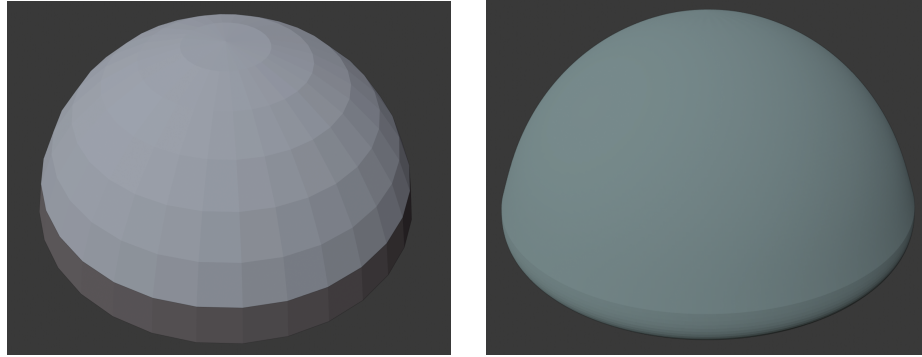


Fig. 2. **Left:** Discrete layers of soft robot. **Right:** Soft robot in a Gaussian curvature.

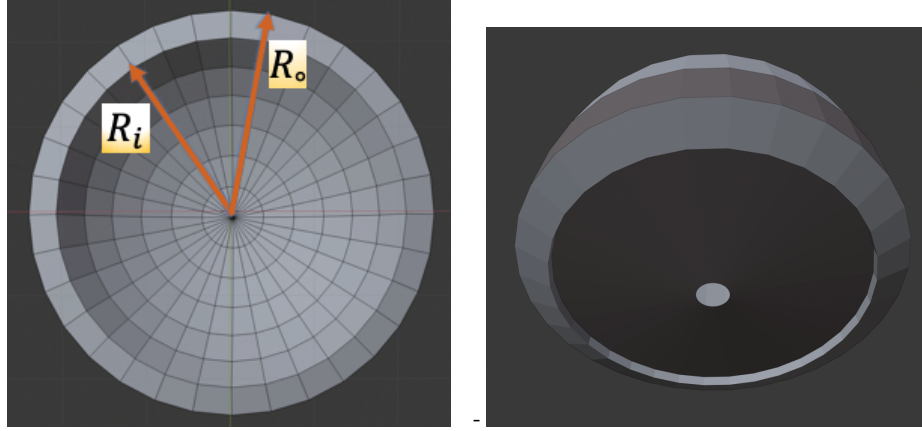


Fig. 3. **Left:** Hollow actuation chamber in reference configuration with internal and external radii, $\{R_i, R_o\}$. **Right:** Back cover (exterior) and side cross-section.

Fig. 4. Head Coordinate System.

2.3 Mass, Inertia Momenta and Center of Gravity of Human Head Model

Following [38]’s study that quantified the mass, volume and center of gravity of the human head using cadavers, we choose the following values for the inertial mass and density properties for the head, neck and torso model we use in our simulations. The head coordinate system is described with the z axis positive along the superior plane and pointing up, the x forward and positive anteriorly through a plane horizontal to the most inferior of the right inferior orbital margin, and y being the cross-product of x and z as shown in Figure 4 – essentially a line through the midpoint of the external auditory meatuses and perpendicular to the midsagittal plane. The head origin has its midpoint at the center of the line between the auditory meatuses, a point in the mid-sagittal plane. Based on the calculations of [37, 38], and [3], we choose the following table shows an illustrative example of the range of the head unit as well as head and neck unit mass, volume, and specific gravity for a typical adult whose age are in the range

49.31 – 69 years, stature in the range, 169.4 ~ 174.8cm, and weights in the range 57.99 66.52kg We will be leveraging the properties listed in [Table 2](#) in our experiments

H+N M	H+N SG	H M	H SG	H+N CM (cm)	H+N CM (°)
6 ± .79	1.125 ± .1	4.37 ± .59	1.11 ± .088	.2 ~ 1.6	96 ~ 303
H CM (cm)	H CM (°)	H+N $I_{yy}(kgm^{-2})$		H $I_{yy}(kgm^{-2})$	
1.3 ~ 3.6	269 ~ 315.5	.357 ~ .567		.157 ~ .323	

Table 2. Head and neck (H+N) unit and head (H) mass, inertia, and specific gravity properties reproduced from [\[38\]](#)

section.

2.4 Type and Number Synthesis for 6-DOF Grasping Soft Mechanisms

The soft robots and IAB system is shown in [Figure 5](#).

Here, we want to study the freedom, and constraints as well as the structural analysis of the kinematic chains. Heavily refer to Chapter 2 of [\[11\]](#)

Here, we dimension the mechanism by the main dimensions and geometrical proportions. Graphical constructions and computer-aided analysis

Advantages of my underactuated mechanism compared to Rodney and other researchers' mechanism.

Here, we describe the constraint connection between the head and soft robots.

2.5 Dimensional Synthesis for 6-DOF Spherical Grasping Soft Mechanisms

2.6 Fully-actuated vs Underactuated Mechanisms

2.7 Nonholonomic Contact Profile Design

The IABs change their configuration based on air that flows into or out of their air chambers when the sensed deviation of the patient from a target exceeds a pose setpoint or a desired trajectory path. The degrees of freedom of the mechanism can be determined using *Gruëbler-Kutzbach's mobility condition*, wherein the number of degrees of freedom, or for short freedom, of the mechanism is given by

$$F = 3(n - g - 1) + \sum_{i=1}^g f_i \quad (1)$$

where n is the number of links in the mechanism, g is the number of joints, f_i is the total number of degrees of freedom for the i th joint given the planar motion associated with the freedoms of the joints. Therefore, we have through (1) that the mechanism has 8 dofs.

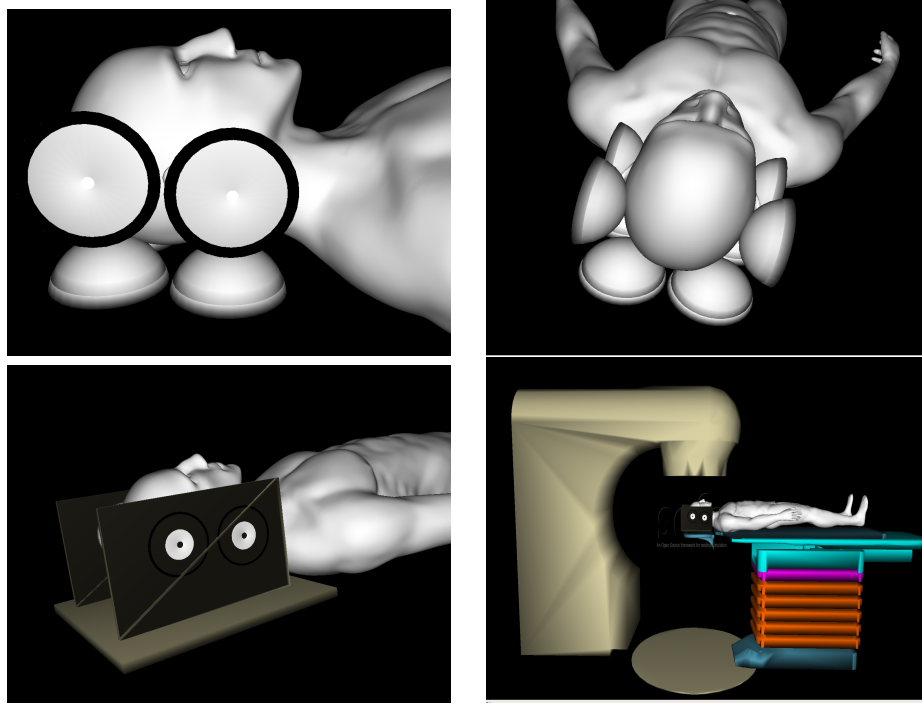


Fig. 5. System setup. **Top Left:** Side view of soft manipulators around H&N region while a patient lies in a supine position. **Top Right:** Top-down view of system setup. **Bottom Left:** Carbon nanotube IAB holder, preventing slippage of head around IABs. This system is 100% radiation transparent and typically used in H&N radiation therapy delivery. **Bottom Right:** Overall setup with gantry, turntable and couch system. [Image best visualized in colored ink].

3 Deformation Analysis

In this section, we present the deformation analysis of the hemispherical IABs based on mechanism Type I of § 2. We analyze the stress laws and constitutive relations that govern their deformation and conclude the section by solving the boundary value problem under the assumptions of *incompressibility* of the isotropic elastic IAB material and the inextensible mesh that constrains the deformation along the circumferential directions. We present the kinematics of the IAB based on a relationship between internal pressure, Cauchy stress, stored strain energy, and the position vector of the IAB, *i.e.* (33). We make the assumption that volume does not change locally during deformation at a configuration $\chi(t)$ at time t . We work from a continuum mechanics framework, whereby we consider only final configurations of the soft robot. For a background material on this section, we refer readers to [24, §2-§3] and [19]. The commonly used notations throughout the rest of this paper is listed in Table 1.

3.1 Nonlinear Elastic Deformation Model

As we are dealing with fluids in the chambers of the IABs, *we use the Eulerian specification in our stress field equations*. Forces that produce deformations are derived using the strain energy-invariants relationship. For readers implementing these principles on solids or hyperelastic materials, a Lagrangean formulation may be appropriate since a reference configuration may be chosen to coincide with the geometry of the solid initially.

Suppose that circular fibers (made out of non-woven fabric materials) are embedded within the elastomeric IAB volume as a reinforcement for conformal radially symmetric deformation. Further, suppose that the elastic properties of the elastomer matrix and fiber reinforcing are described in terms of the strain-energy functions Ψ_{iso} and Ψ_{mesh} respectively. Choosing a Mooney-Rivlin formulation [16,30], we find that Ψ_{iso} depends on the elastomeric invariants I_1 , and I_2 which are functions of the principal stretches, $\lambda_r, \lambda_\phi, \lambda_\theta$ *i.e.*,

$$I_1 = \mathbf{tr}(\mathbf{C}) = \lambda_r^2 + \lambda_\phi^2 + \lambda_\theta^2, \quad \text{and} \quad I_2 = \mathbf{tr}(\mathbf{C}^{-1}) = \lambda_r^{-2} + \lambda_\phi^{-2} + \lambda_\theta^{-2}, \quad (2)$$

where $\lambda_r \lambda_\phi \lambda_\theta = 1$ following the incompressibility assumption of the elastomeric IAB material [33]. The Mooney-Rivlin strain energy for small deformations as a function of the strain invariants of (2) is

$$\Psi_{\text{iso}}(I_1, I_2) = \frac{1}{2}C_1(I_1 - 3) + \frac{1}{2}C_2(I_2 - 3). \quad (3)$$

Similarly, the strain energy of the fiber along a direction \mathbf{M} in the reference configuration is a function of $I_4 = \mathbf{M} \cdot \mathbf{CM}$, where the symbol “.” denotes the dot product. We choose the standard reinforcing model for the fabric membrane *i.e.*,

$$\Psi_{\text{mesh}}(I_4) = \frac{C_4}{2}(I_4 - 1)^2 \quad (4)$$

where C_4 is the fiber stiffness. We thus have the total energy of the elastomer-fiber composite as

$$\Psi(I_1, I_2, I_4) = \Psi_{\text{iso}}(I_1, I_2) + \Psi_{\text{mesh}}(I_4). \quad (5)$$

To find a closed-form expression for I_4 , we consider a strip of the IAB material in the axial/circumferential plane at configuration \mathcal{B} with membranes arranged with respect to the axes indicated in Figure 6. The matrix form of \mathbf{M} is

$$\mathbf{M} = \begin{bmatrix} \cos \gamma & \sin \gamma & 0 \end{bmatrix}^T \quad (6)$$

where γ is the angle between the radial direction and the direction of the fiber family. If there is a deformation, we must have

$$\mathbf{m} = \begin{bmatrix} \lambda_r \cos \gamma & \lambda_\phi \sin \gamma & 0 \end{bmatrix}^T. \quad (7)$$

so that the fiber invariant is,

$$I_4 = \mathbf{M} \cdot \mathbf{CM} = \left[\frac{R^8}{r^8} \cos^2 \gamma \quad \left(\frac{1}{R} + \frac{r}{R} \right)^3 \sin^2 \gamma \quad 0 \right]^T. \quad (8)$$

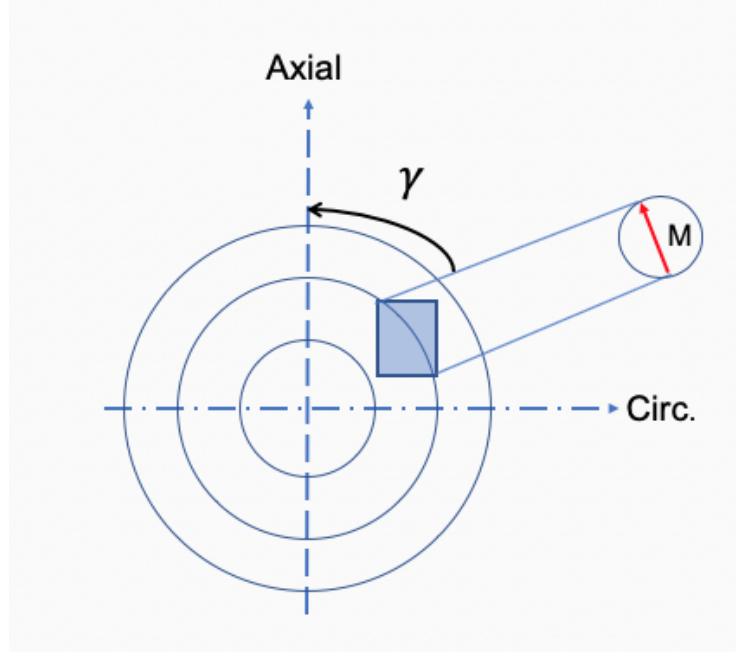


Fig. 6. Fiber-reinforced IAB strip with fibers at angles γ with respect to its axes.

3.2 Strain Analysis: The Deformation Gradient

Here, we derive the deformation gradient of the isotropic component of the strain energy matrix. Suppose a particle on the IAB material surface in the reference configuration has coordinates (R, Φ, Θ) defined in spherical polar coordinates, where R represents the radial distance of the particle from a fixed origin, Θ is the azimuth angle on a reference plane through the origin and orthogonal to the polar angle, Φ . Denote the internal and external radii as R_i , and R_o respectively. We define the following reference configuration constraints,

$$R_i \leq R \leq R_o, \quad 0 \leq \Theta \leq 2\pi, \quad 0 \leq \Phi \leq \pi/2. \quad (9)$$

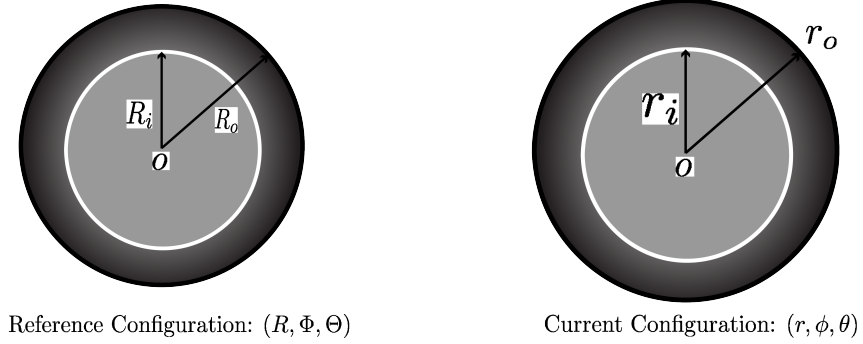
with corresponding current configuration constraints

$$r_i \leq r \leq r_o, \quad 0 \leq \theta \leq 2\pi, \quad 0 \leq \phi \leq \pi/2. \quad (10)$$

The radial vectors \mathbf{R} and \mathbf{r} are given as

$$\mathbf{R} = \begin{pmatrix} R \cos \Theta \sin \Phi, \\ R \sin \Theta \sin \Phi, \\ R \cos \Phi \end{pmatrix} \quad \text{and} \quad \mathbf{r} = \begin{pmatrix} r \cos \theta \sin \phi, \\ r \sin \theta \sin \phi, \\ r \cos \phi \end{pmatrix}. \quad (11)$$

The material volume $\frac{2}{3}\pi(R^3 - R_i^3)$ contained between the IAB walls (of radii R and R_i) remains constant throughout deformation, equal in volume to $\frac{2}{3}\pi(r^3 - r_i^3)$ so that

**Fig. 7.** Radii change under deformation.

the homogeneous deformation between the two configurations and isochoricity imply that

$$r^3 = R^3 + r_i^3 - R_i^3, \quad \theta = \Theta, \quad \phi = \Phi. \quad (12)$$

For bases $\{e_x\}$ and $\{e_X\}$ (with respect to an observer) in the current and reference configurations respectively, we introduce the gradient operator (in the Lagrangean axes) for a fiber element $\mathbf{dx} = \mathbf{dx}_r e_r + \mathbf{dx}_\phi e_\phi + \mathbf{dx}_\theta e_\theta$ (in Eulerian axes) as

$$\nabla = e_R \frac{\partial}{\partial R} + e_\Phi \frac{1}{R} \frac{\partial}{\partial \Phi} + e_\Theta \frac{1}{R \sin \Phi} \frac{\partial}{\partial \Theta}. \quad (13)$$

The deformation gradient, \mathbf{F} , as a dyadic product of a material line element in the current configuration and the gradient operator of (13) is

$$\begin{aligned} \mathbf{F} &= \mathbf{dx} \otimes \nabla \\ &= (\mathbf{dx}_r e_r + \mathbf{dx}_\phi e_\phi + \mathbf{dx}_\theta e_\theta) \otimes \left(e_R \frac{\partial}{\partial R} + e_\Phi \frac{1}{R} \frac{\partial}{\partial \Phi} + e_\Theta \frac{1}{R \sin \Phi} \frac{\partial}{\partial \Theta} \right). \end{aligned} \quad (14)$$

We can verify that the following deformation gradient relation holds (using (12) as a representative fiber material)

$$\mathbf{F} = \begin{pmatrix} \frac{R^2}{r^2} & -\frac{\phi}{R} & -\frac{\theta}{R} \\ 0 & \frac{r}{R} + \frac{1}{R} & -\frac{\theta}{R} \cot \phi \\ 0 & 0 & \frac{r}{R} + \frac{\phi}{R} \cot \phi + \frac{1}{R \sin \Phi} \end{pmatrix} \quad (15)$$

(see Appendix A for the derivation). The principal stretches are given by

$$\lambda_r = \frac{R^2}{r^2}; \quad \lambda_\phi = \frac{r}{R} + \frac{1}{R}; \quad \lambda_\theta = \frac{r}{R} + \frac{\phi}{R} \cot \phi + \frac{1}{R \sin \Phi} \quad (16)$$

with the associated right and left Cauchy-Green tensors

$$\mathbf{C} = \mathbf{B} = \begin{bmatrix} \frac{R^4}{r^4} & 0 & 0 \\ 0 & \left(\frac{1}{R} + \frac{r}{R}\right)^2 & 0 \\ 0 & 0 & \left(\frac{r}{R} + \frac{\phi}{R} \cot \phi + \frac{1}{R} \csc \phi\right)^2 \end{bmatrix} \quad (17)$$

3.3 Stress Response from Strain Energy

We are concerned with the magnitudes of the differential stress on the IAB shells from a mechanical point of view and *our approach is based on a continuum mechanics viewpoint which is independent of finite element methods*. Since the IAB deforms at ambient temperature, we take thermodynamic properties such as temperature and entropy to have negligible contribution. The IAB material stress response, \mathbf{G} , at any point on the IAB's boundary at time t determines the Cauchy stress, $\boldsymbol{\sigma}$, as well as the history of the motion up to and at the time t [19]. The *constitutive equation* that relates the stress to an arbitrary motion will be determined using [36]'s *determinism for the stress principle*. The constitutive relation for the nominal stress deformation for an elastic IAB material is given by

$$\boldsymbol{\sigma} = \begin{pmatrix} \sigma_{rr} & \sigma_{r\theta} & \sigma_{r\phi} \\ \sigma_{\theta r} & \sigma_{\theta\theta} & \sigma_{\theta\phi} \\ \sigma_{\phi r} & \sigma_{\phi\theta} & \sigma_{\phi\phi} \end{pmatrix} = \mathbf{G}(\mathbf{F}) + q\mathbf{F} \frac{\partial \Lambda}{\partial \mathbf{F}}(\mathbf{F}), \quad (18)$$

where \mathbf{G} is a functional with respect to the configuration χ , q acts as a Lagrange multiplier, and Λ denotes the internal (incompressibility) constraints of the IAB system. For an incompressible material, the indeterminate Lagrange multiplier becomes the hydrostatic pressure *i.e.* $q = -p$ [10]. The incompressibility of the IAB material properties imply that $\Lambda \equiv \det \mathbf{F} - 1$. We can verify that

$$\boldsymbol{\sigma} = \mathbf{G}(\mathbf{F}) - p\mathbf{I} \quad (19)$$

following the isochoric assumption *i.e.*, $\det(\mathbf{F}) = 1$. In terms of the stored strain energy, we find that

$$\boldsymbol{\sigma} = \frac{\partial \Psi}{\partial \mathbf{F}} \mathbf{F}^T - p\mathbf{I} \quad (20)$$

where \mathbf{I} is the identity tensor and p represents an arbitrary hydrostatic pressure. It follows that the constitutive law that governs the Cauchy stress tensor is

$$\begin{aligned} \boldsymbol{\sigma} &= \frac{\partial \Psi_{\text{iso}}}{\partial \mathbf{I}_1} \frac{\partial \mathbf{I}_1}{\partial \mathbf{F}} \mathbf{F}^T + \frac{\partial \Psi_{\text{iso}}}{\partial \mathbf{I}_2} \frac{\partial \mathbf{I}_2}{\partial \mathbf{F}} \mathbf{F}^T + \frac{\partial \Psi_{\text{mesh}}}{\partial \mathbf{I}_4} \frac{\partial \mathbf{I}_4}{\partial \mathbf{F}} \mathbf{F}^T - p\mathbf{I} \\ &= \frac{1}{2} C_1 \frac{\partial \text{tr}(\mathbf{FF}^T)}{\partial \mathbf{F}} \mathbf{F}^T + \frac{1}{2} C_2 \frac{\partial \text{tr}([\mathbf{F}^T \mathbf{F}]^{-1})}{\partial \mathbf{F}} \mathbf{F}^T + C_4(I_4 - 1) \frac{\partial (\mathbf{M} \cdot \mathbf{CM})}{\partial \mathbf{F}} - p\mathbf{I} \\ &= C_1 \mathbf{FF}^T - C_2 (\mathbf{F}^T \mathbf{F})^{-1} + 2C_4(I_4 - 1)(\mathbf{FM})(\mathbf{FM})^T - p\mathbf{I} \\ \boldsymbol{\sigma} &= C_1 \mathbf{B} - C_2 \mathbf{C}^{-1} + 2C_4(I_4 - 1)\mathbf{FM} \otimes \mathbf{FM} - p\mathbf{I}. \end{aligned} \quad (21)$$

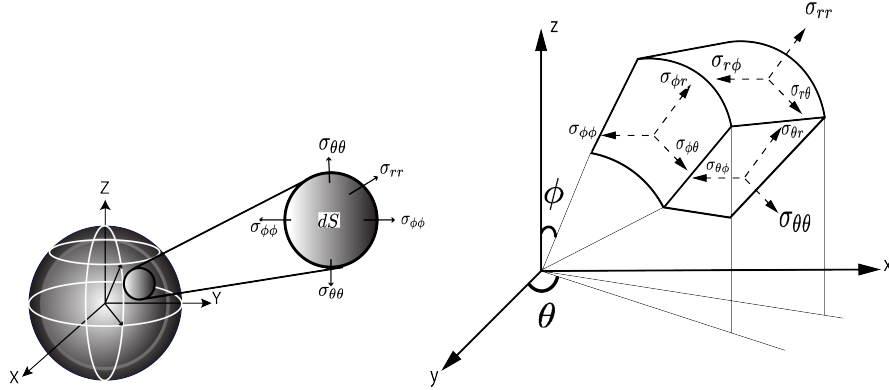


Fig. 8. Stress distribution on the IAB's differential surface, dS .

Examining the structure of (21), we see that the shear stress components vanish; so that the normal stress components are given by

$$\sigma_{rr} = -p + \frac{R^4}{r^4} C_1 - \frac{r^4}{R^4} C_2 - 2C_4 \frac{R^8}{r^8} \cos^2 \gamma + 2C_4 \frac{R^{16}}{r^{16}} \cos^4 \gamma \quad (22a)$$

$$\sigma_{\phi\phi} = -p + \frac{(1+r)^2}{R^2} C_1 - \frac{R^2}{(1+r)^2} C_2 - 2C_4(1+r)^4 \sin^2 \gamma \frac{(R^4 - (1+r)^4 \sin^2 \gamma)}{R^8} \quad (22b)$$

$$\sigma_{\theta\theta} = -p + \frac{(r + \phi \cot \phi + \csc \phi)^2}{R^2} C_1 - \frac{R^2}{(r + \phi \cot \phi + \csc \phi)^2} C_2. \quad (22c)$$

Additionally, $\sigma_{\theta\theta} = 0$ owing to the circumferential constraint provided by the fabric membrane so that only σ_{rr} and $\sigma_{\phi\phi}$ contribute to the constitutive stress law. A visualization of the component stresses of (22) on the outer shells of the IAB material is illustrated in Figure 8.

3.4 Boundary-Value Problem

The dynamic problem is to find the stress at every point in the robot's body subjected to external forces under suitable boundary conditions. The soft elastic materials are normally positioned around the object so that body forces are applied only along the axial direction; the fixed direction of axial loading implies that the deformation is a function of conservative forces only so that uniqueness of solution of stress field equations are preserved owing to Kirchoff's theorem [5, §7.4]. Furthermore, we assume that the applied pressure does not exceed a threshold that makes the rubber material yield to the point of buckling – thus, simplifying the solutions of the ensuing partial differential equations. The equilibrium equations for the physical component vectors of the body

force, $\mathbf{b} = \{b_r, b_\phi, b_\theta\}$ are (see [22])

$$-b_r = \frac{1}{r^2} \frac{\partial(r^2 \sigma_{rr})}{\partial r} + \frac{1}{r \sin \phi} \frac{\partial(\sin \phi \sigma_{r\phi})}{\partial \phi} + \frac{1}{r \sin \phi} \frac{\partial}{\partial \theta} \sigma_{r\theta} - \frac{1}{r} (\sigma_{\theta\theta} + \sigma_{\phi\phi}) \quad (23a)$$

$$-b_\phi = \frac{1}{r^3} \frac{\partial(r^3 \sigma_{r\phi})}{\partial r} + \frac{1}{r \sin \phi} \frac{\partial(\sin \phi \sigma_{\phi\phi})}{\partial \phi} + \frac{1}{r \sin \phi} \frac{\partial(\sigma_{\theta\phi})}{\partial \theta} - \frac{\cot \phi}{r} (\sigma_{\theta\theta}) \quad (23b)$$

$$-b_\theta = \frac{1}{r^3} \frac{\partial(r^3 \sigma_{\theta\theta})}{\partial r} + \frac{1}{r \sin^2 \phi} \frac{\partial(\sin^2 \phi \sigma_{\theta\phi})}{\partial \phi} + \frac{1}{r \sin \phi} \frac{\partial}{\partial \theta} \sigma_{\theta\theta}. \quad (23c)$$

Owing to the CCOARSE symmetry of the elastic solid IAB materials, all shearing stresses, $\sigma_{r\theta}, \sigma_{\phi\theta}, \sigma_{r\phi}$ etc., vanish. We set the following boundary conditions for the normal stresses

$$\sigma_{rr}|_{r=r_o} = -P_{\text{atm}}, \quad \sigma_{rr}|_{r=r_i} = -P_{\text{atm}} - P \quad (24)$$

where P_{atm} is the atmospheric pressure and $P > 0$ is the internal pressure exerted on the internal walls of the IAB above P_{atm} i.e., $P > P_{\text{atm}}$. Furthermore, we note that $\sigma_{\theta\theta} = 0$ owing to the circumferential constraint. The body forces, b_i , in (23) are the external forces exerted by the object within the workspace of the robots. Thus, (23) becomes

$$-b_r = \frac{1}{r^2} \frac{\partial(r^2 \sigma_{rr})}{\partial r} - \frac{\sigma_{\phi\phi}}{r} \quad (25a)$$

$$-b_\phi = \frac{1}{r \sin \phi} \frac{\partial}{\partial \phi} (\sin \phi \sigma_{\phi\phi}), \quad -b_\theta = 0. \quad (25b)$$

Expanding (25a) and substituting (24), we can verify that

$$P = \int_{r_i}^{r_o} \frac{1}{r} (rb_r + \sigma_{\phi\phi} - 2\sigma_{rr}) dr \quad (26)$$

where r , and b_r are known. Under the incompressibility properties of the IAB material we have,

$$r^3 = R^3 + r_i^3 - R_i^3, \quad \text{and } r_o^3 = R_o^3 + r_i^3 - R_i^3. \quad (27)$$

We say equations (26), and (27) completely determine the inverse kinematics (SOFT IK) of the IAB material: given a desired expansion or compression of the IAB walls, it determines the internal pressurization as well as torsional stress necessary to achieve a particular radially symmetric deformation.

3.5 Deformation in Generalized Coordinates

At a material point \mathbf{X} of the IAB surface in a configuration \mathcal{B}_o , it can be verified that the tensor $\mathbf{C} - \mathbf{I}$ represents a change in length of an arbitrary line element of the material. For the material not to be strained, we must have the Lagrangean strain tensor (strain rate) as zero i.e. $\mathbf{E} = \frac{1}{2}(\mathbf{C} - \mathbf{I}) = 0$. A particle \mathbf{X} 's displacement from the reference

to the current configurations must be such that the point difference $d = \mathbf{x} - \mathbf{X}$ is $d(\mathbf{X}) = \chi(\mathbf{X}) - \mathbf{X}$, where $\chi(\mathbf{X})$ follows the notations of [19, 22, 24]. We therefore characterize the point differences by the two-point *displacement gradient*,

$$\mathbf{D} = \text{Grad } d(\mathbf{X}) = \mathbf{F} - \mathbf{I}. \quad (28)$$

If we define unit vectors \mathbf{m} and \mathbf{M} tangent to material line elements \mathbf{dx} and \mathbf{dX} in the current and reference configurations respectively¹, it follows from the invariant of deformation that

$$\mathbf{m}|\mathbf{dx}| = \mathbf{FM}|\mathbf{dX}| \implies |\mathbf{dx}|^2 = \mathbf{M} \cdot (\mathbf{CM})|\mathbf{dX}|^2. \quad (29)$$

Whence, the *stretch* between line elements \mathbf{dx} and \mathbf{dX} is

$$\lambda(\mathbf{M}) = \frac{|\mathbf{dx}|}{|\mathbf{dX}|} = |\mathbf{FM}| \equiv (\mathbf{M} \cdot (\mathbf{CM}))^{\frac{1}{2}}. \quad (30)$$

Lastly, we define two line elements \mathbf{dX} and \mathbf{dX}' with unit tangent vectors \mathbf{M} and \mathbf{M}' at points \mathbf{X} and \mathbf{X}' in the reference configuration; these fibers correspond to \mathbf{dx} and \mathbf{dx}' with unit vectors \mathbf{m} and \mathbf{m}' at points \mathbf{x} and \mathbf{x}' in the current configuration. Let β denote the angle between the directions \mathbf{M} and \mathbf{M}' and let α be the angle between directions \mathbf{m} and \mathbf{m}' ; then

$$\mathbf{dx} = \mathbf{FdX}, \quad \mathbf{dx}' = \mathbf{FdX}', \quad \beta = \cos^{-1}(\mathbf{M} \cdot \mathbf{M}'), \quad (31a)$$

$$\text{and } \alpha = \cos^{-1}(\mathbf{m} \cdot \mathbf{m}') = \cos^{-1}(\mathbf{M} \cdot (\mathbf{CM}')/\lambda(\mathbf{M}) \cdot \lambda(\mathbf{M}')). \quad (31b)$$

In the plane of shear of \mathbf{M} and \mathbf{M}' , the *angle of shear* between the material line elements is the reduction in angles

$$\phi = \beta - \alpha. \quad (32)$$

Examining (28), and (30), we notice that they are both characterized by the stretch $\lambda = r/R$ and the radius in the current configuration (c.f. [22]). Therefore, we take the kinematic quantities that characterize the IAB deformation as

$$\mathbf{r} = \begin{bmatrix} \lambda \\ \phi \end{bmatrix} = \begin{bmatrix} r/R \\ \beta - \alpha \end{bmatrix} \quad (33)$$

i.e. \mathbf{r} is a function of material stretch, and the angle of shear between material line elements.

4 Object-IAB Contact Kinematics Analysis

The interactions among the manipulators and head is considered as a classical case of two elastic bodies in contact. Using the soft finger contact primitive [18] as a convex

¹ \mathbf{dx} and \mathbf{dX} are respectively the material line elements at the points \mathbf{x} and \mathbf{X} in their respective configurations i.e. $\mathcal{B}_0, \mathcal{B}$.

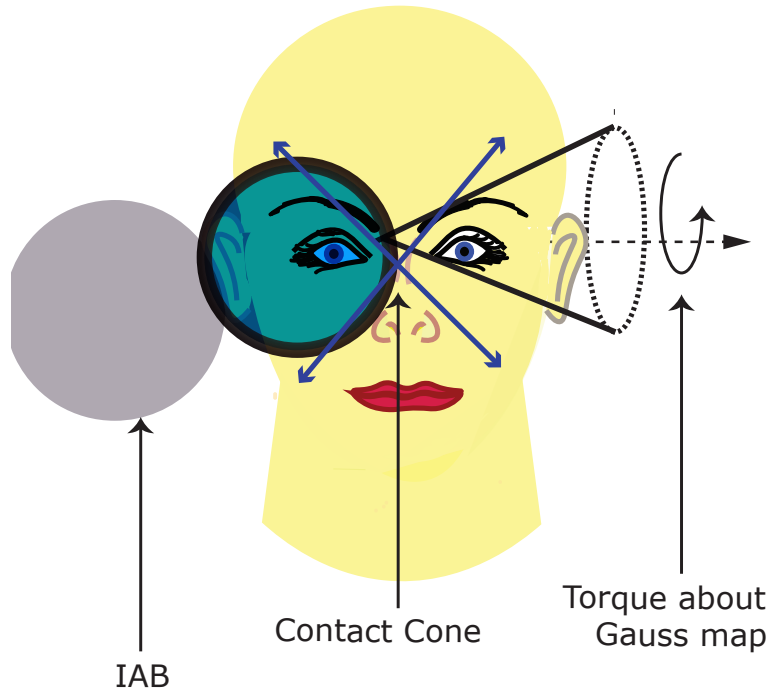


Fig. 9. Soft Contact Illustration

sum of *point contacts* with friction over the area of contact, the IAB forces and torques are modeled within a “cone of forces” about the direction of the surface normal from a patient’s head (see [Figure 9](#)). The trajectory of the head under the influence of motion of an IAB is influenced by the position vector \mathbf{r} ([33](#)). When the IAB deforms, body forces over its current configuration and contact (*traction*) forces over its boundary $\partial\mathcal{B}$ impact motion on the head. Constrained by the frictional coefficient, we define the soft contact force inside the friction cone as

$$\tilde{\mathbf{F}}_{c_i} = \begin{pmatrix} \mathbf{I} & 0 \\ 0 & n_{c_i} \end{pmatrix} \begin{pmatrix} f_{c_i} \\ \tau_{c_i} \end{pmatrix}, \quad (34)$$

where $f_{c_i} \in \mathbb{R}^3$ denotes the amount of force exerted by the IAB along the direction of contact, $\tau_{c_i} \in \mathbb{R}$ is the moment of the contact force, and n_{c_i} is the *normal* or *Gauss map*² for a manifold $S \subset \mathbb{R}^3$ of a head surface. For contact models with friction, we require that all contact forces lie within the friction cone, determined by the frictional coefficient. The set of forces within or on the boundary of the friction cone is

$$FC = \{f_c \in \mathbb{R}^n : \|f_{c_{ij}}^t\| \leq \mu_{ij} \|f_{c_i}^n\|, \\ i = 1, \dots, k, j = 1, \dots, m_i\} \quad (35)$$

where $f_{c_{ij}}^t$ is the tangent component of the j^{th} element of the contact force, $f_{c_i}^n$ is i^{th} contact's normal force, and μ_{ij} is $f_{c_{ij}}$'s coefficient of friction.

4.1 Contact Forces, IAB Stress Components, and Head Gravitational Force

Here, we relate the microscopic contact stress of the previous section with the macroscopic descriptions of the contact friction to enable us treat different material combinations for the manipulator and head. We assume that the stress vector σ at a point on the IAB surface is uniform and continuous throughout the IAB boundary so that it linearly depends on the normal map (this follows from Cauchy's theorem; readers may see the proof in [19, §3.3.1]). Recall that the correspondence between material line, $\{\mathbf{dx}, \mathbf{dX}\}$, elements in the reference and current configuration is

$$\mathbf{dx} = \mathbf{F} \mathbf{dX} \implies \mathbf{F}^{-T} \mathbf{dx} = \mathbf{dX}. \quad (36)$$

where \mathbf{F} is the deformation gradient. Let $\mathbf{H} = \mathbf{F}^{-T}$ and \mathbf{dA} represent an infinitesimal vector element on the material surface at a neighborhood of point \mathbf{X} in \mathcal{B} such that $\mathbf{dA} = \mathbf{N} dA$, where \mathbf{N} is the unit outward normal to the IAB boundary $\partial\mathcal{B}_o$ in the reference configuration. The corresponding deformed surface of the IAB with normal \mathbf{n} from a surface, da , of the IAB in the current configuration is $\mathbf{da} = \mathbf{n} da$. Using *Nanson's formula*, we have the following relation between surfaces in the reference and current configuration

$$\mathbf{da} = J \mathbf{H} \mathbf{dA} \implies \mathbf{n} da = J \mathbf{H} \mathbf{N} dA. \quad (37)$$

where $J = \det \mathbf{F}$. Multiplying throughout equation (37) by the derived constitutive relation between the stress-strain relationship of [22], the resultant contact force on the boundary $\partial\mathcal{B}$ in the current configuration may be written as (owing to the volume preservation on the boundary of the IAB material)

$$\int_{\partial\mathcal{B}} \boldsymbol{\sigma} \mathbf{n} da = \int_{\partial\mathcal{B}_o} J \boldsymbol{\sigma} \mathbf{H} \mathbf{N} dA. \quad (38)$$

We may define the *Piola-Kirchoff* stress tensor field as

$$\mathbf{S} = J \mathbf{H}^T \boldsymbol{\sigma} \quad (39)$$

² A normal map for a manifold S is a continuous map $g : S \rightarrow S^2 \subset \mathbb{R}^3$ such that for every $s \in S$, $g(s)$ is orthogonal to S at s [15].

so that the force on an element surface \mathbf{da} of the IAB in a configuration \mathcal{B} is

$$\boldsymbol{\sigma} \mathbf{da} = \mathbf{S}^T \mathbf{dA}.$$

Thus, the contact force f_{c_i} on an element surface \mathbf{dA} of the i^{th} IAB in a configuration \mathcal{B} (as in (34)) is

$$f_{c_i} = \mathbf{S}_i^T \mathbf{dA}_i = J_i \boldsymbol{\sigma}_i \mathbf{H}_i \mathbf{dA}_i = J_i \boldsymbol{\sigma}_i \mathbf{F}_i^{-1} \mathbf{dA}_i \quad (40)$$

where (40) follows from the symmetric property of \mathbf{F}_i and $\boldsymbol{\sigma}_i$. For the i^{th} IAB, at the region of contact, we have the contact force as

$$f_{c_i} = J_i \left(\frac{R_i^2}{r_i^2} P_i + \frac{R_i}{r_i} \sigma_{\phi\phi_i}(\epsilon) + \frac{R_i}{r_i} \sigma_{\theta\theta_i}(\zeta) \right) \mathbf{dA}_i \quad (41)$$

where $\sigma_{jj_i}(v)$ are the definite integrals of (??). Owing to the isochoric deformation assumption, we have from (41) that

$$f_{c_i} = \left(\frac{R_i^2}{r_i^2} P_i + \frac{R_i}{r_i} \sigma_{\phi\phi_i}(\epsilon) + \frac{R_i}{r_i} \sigma_{\theta\theta_i}(\zeta) \right) n_{c_i} dA_i. \quad (42)$$

where we have set the outward normal map \mathbf{N} to n_{c_i} of (34). The torque is the moment of the contact force on the i^{th} IAB, and it is given by

$$\boldsymbol{\tau}_{c_i} = f_{c_i} \times r_{c_i} \quad (43)$$

where $r_{c_i} \in \mathbb{R}^3$ is the unit vector between the head reference point and the contact. The soft contact force of (34) can be re-stated in terms of the derived stress tensor, the deformation gradient (see [22]) and the Piola-Kirchoff stress field of (39) *i.e.*

Friction Cones' Contact Force

$$\tilde{F}_{c_i} = \begin{bmatrix} \mathbf{I} & 0 \\ 0 & n_{c_i} \end{bmatrix} \begin{bmatrix} f_{c_i} \\ f_{c_i} \times r_{c_i} \end{bmatrix}. \quad (44)$$

where f_{c_i} and $\boldsymbol{\tau}_{c_i}$ are as given in equations (42) and (43).

4.2 Contact Coordinates and Head Velocity

The head will make contact with the IAB at multiple points on its surface, so we describe the kinematics of these contact points using an atlas³ of contact coordinate charts. In this sentiment, let C_{r_1} and C_{r_n} respectively represent a fixed reference frame with respect to the IAB and head, H (see Figure 10). Furthermore, let $S_1 \subset \mathbb{R}^3$

³ An atlas \tilde{S} is a set of surfaces where each surface $S \in \tilde{S}$ has an invertible map $f(\mathbf{u})$ from an open subset U of \mathbb{R}^2 to a surface $S \subset \mathbb{R}^3$ such that the partial derivatives $\frac{\partial f}{\partial u}(\mathbf{u}), \frac{\partial f}{\partial v}(\mathbf{v})$ are linearly independent for all $\mathbf{u} = (u, v) \in U$.

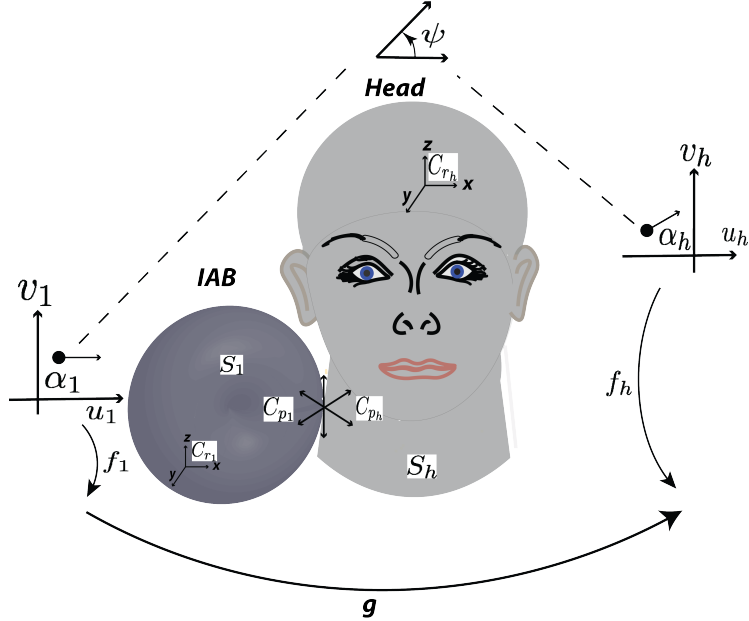


Fig. 10. Sliding and rolling contact illustration of a single IAB and the Head. [Image best visualized in colored ink].

and $S_h \subset \mathbb{R}^3$ denote the respective *orientable manifold*⁴ embeddings of the IAB and head surfaces with respect to frames C_{r_1} and C_{r_h} . We shall let S_1 and S_r belong to the *atlases* $\{S_{1_i}\}_{i=1}^{n_1}$, $\{S_{h_j}\}_{j=1}^{n_r}$ respectively. Suppose (f_1, U_1) and (f_r, U_r) are *coordinate systems* for the IAB and the head respectively, where f_i is an invertible map, $f_i(u_i, v_i) : U \rightarrow S_i \subset \mathbb{R}^3$

$$f_i(u_i, v_i) : \{U \rightarrow S_i \subset \mathbb{R}^3 | i = 1, h\},$$

from an open subset U of \mathbb{R}^2 to a *coordinate patch* $S_i \subset \mathbb{R}^3$ such that the partial derivatives $\frac{\partial f_i}{\partial u_i}$ and $\frac{\partial f_i}{\partial v_i}$ are linearly independent. Let $p_1(t) \in S_1$ and $p_h(t) \in S_h$ represent the positions of the contact points with respect to frames C_{r_1} and C_{r_h} respectively at time t . In general, the contact points $p_1(t)$ and $p_h(t)$ will not remain in the coordinate systems S_1 and S_h for all time. Thus, we choose an interval I where $p_1(t) \in S_{1_i}$ and $p_h(t) \in S_{h_j}$ for all $t \in I$ and some i and j . As seen in Figure 10, C_{p1} and C_{ph} denote the contact frames that coincide with the *normalized Gauss frames* at p_1 and p_h for all $t \in I$, and α_1 , α_h are local coordinate frames that describe the IAB motion with respect to the head such that

$$\alpha_1 = (u_1, v_1) \in U_1, \text{ and } \alpha_h = (u_h, v_h) \in U_h. \quad (45)$$

⁴ An orientable manifold is a manifold S for which the Gauss map exists.

Let the angle between the tangent planes of α_1 , and α_h be ψ . The transformation matrix $g \in \Omega \subset SE(3)$ encodes the relative orientation and position of the IAB with respect to the head where Ω is the set of all relative positions and orientations in the atlases $\{S_{1_i}\}_{i=1}^{n_1}$, $\{S_{h_i}\}_{i=1}^{n_h}$ for which the IAB and head remain in contact. We let the *contact coordinates* be described by $\eta = (\alpha_1, \alpha_h, \psi)$. The head's motion is governed by traction forces arising from the friction tangential to the IAB surface and the pressure normal to the IAB surface. Thus, at the points of contact, if $R \in SO(3)$ is the rotatory component of g , η must satisfy

$$g \circ f_1(\alpha_1) = f_h(\alpha_h) \quad (46a)$$

$$R n_1(\alpha_1) = -n_h(\alpha_h) \quad (46b)$$

since the contact locations must coincide for the IAB and the head, and the tangent planes must coincide so that the outward normal maps $n_1 : S_1 \rightarrow S^2 \subset \mathbb{R}^3$ and $n_h : S_h \rightarrow S^2 \subset \mathbb{R}^3$ agree. Furthermore, the orientation of the tangent planes of α_1 and α_h is the unique angle $\psi \in [0, 2\pi)$ between the x -axes of C_{p_1} and C_{p_h} such that

$$R \frac{\partial f_1}{\partial \alpha_1} M_1^{-1} R_\psi = \frac{\partial f_h}{\partial \alpha_h} M_h^{-1} \quad (47)$$

where M_i is a 2×2 square root of the Riemannian metric tensor [32] that normalizes the columns of $\frac{\partial f}{\partial \alpha}$, i.e.

$$M_i = \begin{bmatrix} \|\frac{\partial f_i}{\partial u_i}\| & 0 \\ 0 & \|\frac{\partial f_i}{\partial v_i}\| \end{bmatrix} \quad (48)$$

and R_ψ is chosen such that a rotation of C_{p_1} about its z -axis through $-\psi$ radians aligns the x -axes of the local coordinate system α_1 to that of the head's local coordinate system α_h i.e.

$$R_\psi = \begin{bmatrix} \cos \psi & -\sin \psi \\ -\sin \psi & \cos \psi \end{bmatrix} \quad (49)$$

with the special property that $R_\psi = R_\psi^T = R_\psi^{-1}$. We define the normalized Gauss frame at a point u on the surface U of the orthogonal coordinate system (f, U) as,

$$[x_u \ y_u \ z_u] = [\frac{\partial f}{\partial u} / \|\frac{\partial f}{\partial u}\| \ \frac{\partial f}{\partial v} / \|\frac{\partial f}{\partial v}\| \ n_u(f(u))] \quad (50)$$

where x_u , y_u , and z_u are functions mapping $U \subset \mathbb{R}^2 \rightarrow \mathbb{R}^3$ and n_u is the continuous Gauss map $n_u : S \rightarrow S^2 \subset \mathbb{R}^3$. The motion of the contacts $\dot{\eta}$ as a function of components of the twist vector $\hat{\xi} = (v, w)^T$ is given in (51) as the respective *first*, *second*, and *third equations of contact*. Our derivation, which closely follows [17]'s multi-fingered kinematics' proof, may be found in Appendix C.

$$\dot{\alpha}_h = M_h^{-1}(\mathcal{K}_h + \tilde{\mathcal{K}}_1)^{-1} \left(\omega_t - \tilde{\mathcal{K}}_1 v_t \right) \quad (51a)$$

$$\dot{\alpha}_1 = M_1^{-1} R_\psi (\mathcal{K}_h + \tilde{\mathcal{K}}_1)^{-1} (\omega_t - \mathcal{K}_h v_t) \quad (51b)$$

$$\dot{\psi} = \omega_n + T_h M_h \dot{\alpha}_h + T_1 M_1 \dot{\alpha}_1 \quad (51c)$$

where

$$\begin{aligned}
T_h &= y_h^T \frac{\partial x_h}{\partial \alpha_h} M_h^{-1}, \quad T_1 = y_1^T \frac{\partial x_1}{\partial \alpha_1} M_1^{-1}, \\
\mathcal{K}_h &= [x_h^T, y_h^T]^T \frac{\partial n_h^T}{\partial \alpha_h} M_h^{-1}, \quad \omega_n = z_h^T \omega \\
\mathcal{K}_1 &= R_\psi [x_1^T, y_1^T]^T \frac{\partial n_1^T}{\partial \alpha_1} M_1^{-1} R_\psi, \\
\omega_t &= [x_h^T, y_h^T]^T [n_h \times \omega]^T, \\
v_t &= [x_h^T, y_h^T]^T [(-f_h \times \omega + v)]^T. \tag{52}
\end{aligned}$$

Note that ω_t is the rolling velocity of the head projected onto the tangent plane of the contact and v_t is the sliding velocity; ω_n is the relative rotational velocity projected to the contact's surface normal, and $\tilde{\mathcal{K}}_1 = R_\psi \mathcal{K}_1 R_\psi$ is the curvature of the IAB with respect to the contact frame that coincides with the normalized Gauss frame at $p_1(t)$. The matrix $(\mathcal{K}_h + \tilde{\mathcal{K}}_1)^{-1}$ is the so-called *relative curvature* originally coined by [15]. Simplifying (52), we find that

$$\begin{aligned}
x_h &= \frac{\partial f}{\partial u_h} / \left\| \frac{\partial f}{\partial u_h} \right\|, \quad y_h = \frac{\partial f}{\partial v_h} / \left\| \frac{\partial f}{\partial v_h} \right\|, \quad z_h = n_u(f(u)) \\
T_h &= y_h \left[\frac{\partial x_h^T}{\partial u_h} / \left\| \frac{\partial f}{\partial u_h} \right\|, \frac{\partial x_h^T}{\partial v_h} / \left\| \frac{\partial f}{\partial v_h} \right\| \right], \\
T_1 &= y_1 \left[\frac{\partial x_1^T}{\partial u_1} / \left\| \frac{\partial f}{\partial u_1} \right\|, \frac{\partial x_1^T}{\partial v_1} / \left\| \frac{\partial f}{\partial v_1} \right\| \right], \\
\mathcal{K}_h &= [x_h^T, y_h^T]^T \left[\frac{\partial n_h^T}{\partial u_h} / \left\| \frac{\partial f}{\partial u_h} \right\|, \frac{\partial n_h^T}{\partial v_h} / \left\| \frac{\partial f}{\partial v_h} \right\| \right], \\
\mathcal{K}_1 &= [x_1^T, y_1^T]^T \left[\frac{\partial n_1^T}{\partial u_1} / \left\| \frac{\partial f}{\partial u_1} \right\|, \frac{\partial n_1^T}{\partial v_1} / \left\| \frac{\partial f}{\partial v_1} \right\| \right]. \tag{53}
\end{aligned}$$

This is verified in Appendix ???. We see that for the contact interaction between an IAB and the head, for a $U \subset \mathbb{R}^2$ we must choose an appropriate $f_i : U_i \rightarrow S_i \subset \mathbb{R}^3$ in order to characterize the setup.

5 System's Newton-Euler Equations

From Truesdell's *determinism for the stress principle* [36], the Cauchy stress σ at any point in a material at time t for any motion up to time t determines the stress response of the material for any arbitrary motion history up to and including time t . We will derive the dynamics of the IAB system in the *strain field of the deformation*. The potential and kinetic energy of the system are considered to be derived from the constitutive strain field relations that characterize the deformation. We now use Lagrangian deformation analysis to derive the dynamic equations of the continuum multi-IAB system.

For a soft continuum body, there is an enormous amount of particle orientations during deformation; the number of particle states that is physically measurable with

sensors instantaneously in a given configuration is overwhelming. However, we can leverage the constitutive law which describes the macroscopic IAB material behavior with respect to a reference frame, S , at a time, t by completely characterizing it by ten dependent variables viz., three components of the position vector, six component stress tensor variables (the shear and normal stress components), and

5.1 Lagrangian and Euler-Lagrange Equations

Following § 3.5, we are only interested in the final position and orientation of the IAB as a whole rather than the system of particles that characterize a deformation at every time t . When the head exerts a reactive wrench on an IAB, it is natural to expect a dent. The shear angle in (33) should capture the amount of angular deformation. For a kinetic energy T and a potential energy V , the *Lagrangian*, L , of the system in generalized coordinates is the difference between the kinetic and potential energy, *i.e.*

$$L(\mathbf{r}, \dot{\mathbf{r}}) = T(\mathbf{r}, \dot{\mathbf{r}}) - V(\mathbf{r}). \quad (54)$$

The equations of motion for a pneumatic IAB system is of the form

$$\frac{d}{dt} \frac{\partial L}{\partial \dot{\mathbf{r}}_i} - \frac{\partial L}{\partial \mathbf{r}_i} = \boldsymbol{\tau}_i, \quad i = 1, \dots, m \quad (55)$$

where $\boldsymbol{\tau}_i$ is the torque acting on the i^{th} generalized coordinate. Written in matrix form equation, we can write the Euler-Lagrange equation of (55) as

$$\frac{d}{dt} \frac{\partial L}{\partial \dot{\mathbf{r}}} - \frac{\partial L}{\partial \mathbf{r}} = \boldsymbol{\tau}. \quad (56)$$

It now remains to derive the kinetic and potential energies for the IAB material. Let the velocity of an IAB material particle x in the current configuration at time t be $\mathbf{v}(\mathbf{r}, t)$, then the Eulerian velocity gradient tensor can be defined as

$$\boldsymbol{\Gamma} = \text{grad } \mathbf{v}(\mathbf{r}, t). \quad (57)$$

Cauchy's first law of motion (??) will allow us to derive the balance of mechanical energy of the system. Multiplying(??) throughout by $\mathbf{v}(\mathbf{r}, t)$, and abusing notation by dropping the arguments of $\mathbf{v}(\mathbf{r}, t)$, we find that

$$\begin{aligned} & \text{div} (\boldsymbol{\sigma}^T \cdot \mathbf{v}) + \rho \mathbf{b} \cdot \mathbf{v} = \rho \mathbf{v} \cdot \dot{\mathbf{v}} \\ \implies & \text{div} (\boldsymbol{\sigma}^T \mathbf{v}) - \mathbf{tr}(\boldsymbol{\sigma} \boldsymbol{\Gamma}) + \rho \mathbf{b} \cdot \mathbf{v} = \rho \mathbf{v} \cdot \dot{\mathbf{v}}. \end{aligned} \quad (58)$$

where ρ is the mass density of the IAB material body. Following mass conservation, we integrate over volume \mathcal{B} and employ the divergence theorem, so that the above relation yields the *balance of mechanical energy*:

$$\int_{\mathcal{B}} \rho \mathbf{b} \cdot \mathbf{v} dv + \int_{\partial \mathcal{B}} f_\rho \cdot \mathbf{v} da = \frac{d}{dt} \int_{\mathcal{B}} \frac{1}{2} \rho \mathbf{v} \cdot \mathbf{v} dv + \int_{\mathcal{B}} \mathbf{tr}(\boldsymbol{\sigma} \boldsymbol{\Gamma}) dv \quad (59)$$

where f_ρ is the IAB body force density, and the left hand side of the foregoing is the so-called *rate of working of the applied forces*. The symmetry of the stress tensor σ implies that $\text{tr}(\sigma \Gamma) = \text{tr}(\sigma \Sigma)$ where Σ is given in terms of the Eulerian-strain rate tensor, Γ i.e.

$$\Sigma = \frac{1}{2}(\Gamma + \Gamma^T) \quad (60)$$

so that the kinetic energy density and stress power are given by,

$$T(\mathbf{r}, \dot{\mathbf{r}}) = \frac{1}{2}\rho\mathbf{v} \cdot \mathbf{v}, \quad V(\mathbf{r}) = \text{tr}(\sigma \Sigma). \quad (61)$$

5.2 Case I: Euler-Lagrange Equation for Cauchy-Elastic IAB Material

The stress-strain relation for the IAB we have presented are only related through the deformation tensor, implying that the material is Cauchy elastic. For Cauchy elastic materials, the stress power term is not conserved during deformation making integration over the material body \mathcal{B} physically unrealistic [19]. For such materials, we may set the stored strain energy V to an arbitrary constant (e.g. an identity or $V(I) = 0$). We can derive the overall torque dynamics of an IAB system as (see proof in Appendix B)

$$\boldsymbol{\tau} = \underbrace{\begin{bmatrix} \rho/R^2 & 0 & 0 \\ 0 & 9\rho r_i^4/2 & 0 \\ 0 & 0 & \rho \end{bmatrix}}_{M_{iab}} \ddot{\mathbf{r}} + \underbrace{\begin{bmatrix} \rho\dot{r}/R^3 & 0 & 0 \\ 0 & 36\rho r_i^3 \dot{r}_i & 0 \\ 0 & 0 & 0 \end{bmatrix}}_{C_{iab}} \dot{\mathbf{r}} \quad (62)$$

Rewriting equation (62) in terms of the torque for each soft robot, we have the dynamics for IAB j as

$$M_{iabj}(\mathbf{r}^j)\ddot{\mathbf{r}}^j + C_{iabj}(\mathbf{r}^j, \dot{\mathbf{r}}^j)\dot{\mathbf{r}}^j = \boldsymbol{\tau}^j \quad (63)$$

where M_{iabj} and C_{iabj} contain the respective inertia and Coriolis forces for actuator j . Since the IAB material is incompressible, the mass density is uniform throughout the body of the material. In general, we write equation (63) as

$$M_{iab}(\tilde{\mathbf{r}})\ddot{\tilde{\mathbf{r}}} + C_{iab}(\tilde{\mathbf{r}}, \dot{\tilde{\mathbf{r}}})\dot{\tilde{\mathbf{r}}} = \tilde{\boldsymbol{\tau}} \quad (64)$$

where $\tilde{\mathbf{r}} \in \mathbb{R}^{n_1} \times \mathbb{R}^{n_2} \times \dots \mathbb{R}^{n_s}$ gives the generalized coordinates for all the IABs and $\tilde{\boldsymbol{\tau}}$ are the vectorized torques of the individual robots.

5.3 Case II: Euler-Lagrange Equation for Green Elastic IAB Material

For the case where the IAB material body is *Green elastic* or *hyperelastic*⁵, the eulerian form of the stress power expression is

$$V(\mathbf{r}) = \text{tr}(\sigma \Sigma). \quad (65)$$

⁵ An hyperelastic material is one where the strain-energy function exists.

We are mostly interested in the mechanical energy in the current configuration, however, it is worthwhile to note that the equivalent relation in the Lagrangean form is

$$\int_{\mathcal{B}_o} \rho_o \mathbf{b}_o \dot{\chi} dV + \int_{\partial \mathcal{B}_o} (\mathbf{S}^T \mathbf{N}) \dot{\chi} dA = \frac{d}{dt} \int_{\mathcal{B}_o} \frac{1}{2} \rho_o \dot{\chi} \cdot \dot{\chi} dV + \int_{\mathcal{B}_o} \text{tr}(\mathbf{S} \dot{\mathbf{F}}) dV, \quad (66)$$

where \mathbf{S} is the Piola-Kirchoff stress tensor. It follows that,

$$V(\mathbf{r}) = \text{tr}(\mathbf{S} \dot{\mathbf{F}}) \quad (67)$$

for a Green elastic material. Similar to the arguments in § 5.2, we find the torque as (see derivation in Appendix B)

Green-Elastic IAB Material Torque

$$\begin{aligned} \tau = & \frac{\rho \ddot{r}}{R^2} + 9\rho r_i^4 \ddot{r}_i + \rho \ddot{\alpha} + \frac{\rho \dot{r}^2}{R^3} + 36\rho r_i^3 \dot{r}_i^2 \\ & + 4C_1 \left(\frac{2R^3}{r^5} + \frac{r}{R^3} \right) + 4C_2 \left(\frac{2r^3}{R^5} + \frac{R}{r^3} \right). \end{aligned} \quad (68)$$

whereupon the equation may be vectorized as in (64).

6 Multi-IAB Statics and End-Effecto Velocities

At a material point, \mathbf{r} , of the IAB surface in the configuration \mathcal{B} , the 3D position of a point is given by (??). Since deformation is radially symmetric, it follows that the regularity of the IAB in its current configuration, $\chi(\mathbf{r}, t)$, implies that it can be uniformly defined by \mathbf{r} throughout the IAB material body. Similar to [22], we are interested in the final state of the IAB after deformation; the path it takes for us to reach the final configuration is not important to us (since there is no obstacle in the continuum robots' workspace). Thus we drop the time dependence on the configuration and take \mathbf{r} to be the generalized coordinate of the IAB. The configuration space of the IAB with respect to the spatial frame at a certain time can then be described by $g_{st}(\chi) \equiv g_{st}(\mathbf{r}) : \mathbf{r} \rightarrow g_{st}(\mathbf{r}) \in SE(3)$ while the strain state of the IAB is characterized by the strain field

$$\hat{\xi}_i(\mathbf{r}) = g_i^{-1} \frac{\partial g_i}{\partial \mathbf{r}} \in \mathfrak{se}(3) = g_i^{-1} g'_i \quad (69)$$

with the respective g'_i 's being the tangent vector at g_i such that $g'_i \in T_{g_i(\mathbf{r})} SE(3)$. Note that $T_{g_i(\mathbf{r})}$ is the tangent matrix at g_i with associated Lie algebra $se(3) \approx T_e SE(3)$.

6.1 End Effector Forces

From the derived relationship between the head contact coordinates and the relative motion (v_t, ω_t) of the IAB *i.e.* equation (51), we can associate a Jacobian that maps

IAB velocities to head position and orientation. A fundamental assumption in our formulation is that the IABs make contact with the head throughout manipulation, and the manipulation is stable and prehensile. A forward kinematic map from the configuration of the i^{th} IAB, χ_{iab_i} maps from respective IAB configurations to head position and orientation *i.e.* $K_{iab_i} : \chi_{iab_i} \rightarrow SE(3)$. The velocity of the head with respect to a fixed base frame in terms of IAB velocities can be written in terms of the forward kinematics Jacobian:

$$\begin{pmatrix} v_{iab_i} \\ \omega_{iab_i} \end{pmatrix} = \frac{\partial K_{iab_i}}{\partial \mathbf{r}_i} \frac{d\mathbf{r}}{dt} K_{iab_i}^{-1} = \mathbf{J}_i(\mathbf{r}_i) \dot{\mathbf{r}}_i \quad (70)$$

where \mathbf{r}_i is the spatial position of IAB i , and $(v_{iab_i}^T, \omega_{iab_i}^T) \in \mathbb{R}^6$ represents the linear and angular velocity of the i^{th} IAB about its screw basis. In essence, $\mathbf{r}_i \in \mathbb{R}^3$ with its rows of mapped to scalars by an appropriate choice of norm. The contact between the head and the IABs is mapped by the Jacobian

$$\mathbf{J}_{c_i}(\xi_h, \xi_{iab_i}) = \begin{bmatrix} \mathbf{I} & \hat{\mathbf{w}}(r_{c_i}) \\ \mathbf{0} & \mathbf{I} \end{bmatrix} J_{r_i}, \quad (71)$$

where $\mathbf{J}_{c_i} : \dot{\xi}_{r_i} \rightarrow [v_{c_i}^T, w_{c_i}^T]^T$, $r_{c_i} \in \mathbb{R}^3$ is a vector between the head reference point (e.g. the center of mass) and the contact with the i^{th} IAB, ξ_h is the position and relative orientation of the head, ξ_{iab_i} is the position and relative orientation of the i^{th} soft robot in world coordinates, $\hat{\mathbf{w}}(r_{c_i})$ is an anti-symmetric matrix for the vector r_{c_i} , and $\xi_r = (\xi_{r_1}, \xi_{r_2}, \dots, \xi_{r_8})$ are the positions and orientations for each of the 8 IABs. The manipulation map, G_i is made up of matrices of the form

$$G_i(\xi_h, \xi_r) = \begin{bmatrix} \mathbf{I} & \mathbf{0} \\ \hat{\mathbf{w}}(r_{c_i}) & \mathbf{I} \end{bmatrix} B_i(\xi_h, \xi_r), \quad (72)$$

where $B_i(\xi_h, \xi_r)$ is the selection map as defined in [14] for the desired manipulation. The net force on the head is a sum of the individual forces arising from each IAB. Owing to the linearity of each individual IAB's contact force, the resultant head force can be stitched together to form G , *i.e.*

$$\tilde{F}_h = [G_1, \dots, G_8] \begin{pmatrix} \tilde{F}_{c_1} \\ \vdots \\ \tilde{F}_{c_8} \end{pmatrix} = G \tilde{F}_c, \quad (73)$$

where $F_h \in \mathbb{R}^6$ and $F_c \in \mathbb{R}^{m_1} \times \mathbb{R}^{m_2} \times \dots \times \mathbb{R}^{m_8}$. The *internal* or *null forces* is captured by the null space $\mathcal{N}(G)$ of the manipulation map G ; these forces correspond to zero net force on the head of the patient. Each \tilde{F}_{c_i} in (73) is of the form (44).

6.2 End-effector Velocities

We define the velocity constraint dual of (72) as the constraint between the relative velocity of the head and that of the twist velocities of the contact point

$$\begin{pmatrix} \tilde{v}_{c_i} \\ \tilde{\omega}_{c_i} \end{pmatrix} = \begin{bmatrix} \mathbf{I} & \hat{\mathbf{w}}(r_{c_i}) \\ \mathbf{0} & \mathbf{I} \end{bmatrix} \begin{pmatrix} v_{c_h} \\ \omega_{c_h} \end{pmatrix}. \quad (74)$$

For a conjugate twist vector $(v_c^T, \omega_c^T)^T$ to the forces exerted by the IABs, f_c , we have the following

$$\begin{pmatrix} v_c \\ \omega_c \end{pmatrix} = G^T \begin{pmatrix} v_{cp} \\ \omega_{ch} \end{pmatrix}. \quad (75)$$

Given a *selection matrix* $B_i^T(\xi_h, \xi_{iab_i}) \in \mathbb{R}_i^m$ for a particular IAB, where m_i is the range of all the forces and moments for the chosen contact primitive (or union of contact primitives), the *manipulation map* for the i^{th} IAB can be written as,

$$G_i^T(\xi_h, \xi_{iab_i})\xi_h = B_i^T(\xi_h, \xi_{iab_i})\mathbf{J}_{c_i}(\xi_h, \mathbf{r}_{r_i})\dot{\xi}_{iab_i} \quad (76)$$

where \mathbf{J}_{c_i} is the contact Jacobian for the i^{th} actuator, and ξ_h denotes the velocity of the head. For the 8 soft actuators, the manipulation constraint of the system can be written as

$$\begin{bmatrix} G_1^T \\ G_2^T \\ \vdots \\ G_8^T \end{bmatrix} \begin{pmatrix} v_h \\ w_h \end{pmatrix} = \text{diag} \begin{pmatrix} B_1^T \mathbf{J}_{c_1} \\ B_2^T \mathbf{J}_{c_2} \\ \vdots \\ B_8^T \mathbf{J}_{c_8} \end{pmatrix} \begin{pmatrix} \dot{\mathbf{r}}_{iab_1} \\ \dot{\mathbf{r}}_{iab_2} \\ \vdots \\ \dot{\mathbf{r}}_{iab_8} \end{pmatrix}. \quad (77)$$

7 Newton-Euler System of Equations

The dynamics of the head is a form of (64) but without the actuator torques. In local coordinates, it has the form

$$\mathbf{M}_h(\zeta)\ddot{\zeta} + \mathbf{C}_h(\zeta, \dot{\zeta})\dot{\zeta} + \mathbf{N}_h(\zeta, \dot{\zeta}) = 0 \quad (78)$$

with ζ being a local parameterization of the position and orientation of the head in the Lie Group $SE(3)$, and \mathbf{N}_h being the gravitational and frictional forces exerted by/on the head. The head and the multi-DOF IAB system are connected via the manipulation constraint *i.e.*

$$G^T(\zeta, \mathbf{r})\dot{\zeta} = \mathbf{J}(\zeta, \mathbf{r})\dot{\mathbf{r}}. \quad (79)$$

Suppose that the velocity constraint produces a virtual displacement constraint in $\delta\zeta$ and $\delta\mathbf{r}$ such that for $q = (\zeta, \mathbf{r})$, we have

$$\delta\mathbf{r} = \mathbf{J}^{-1}(q)G^T(q)\delta\zeta$$

the Lagrange equations become

$$\left(\frac{d}{dt} \frac{\partial L}{\partial \dot{q}} - \frac{\partial L}{\partial q} - (\boldsymbol{\tau}, 0) \right) \delta q = 0 \quad (80a)$$

$$\left(\frac{d}{dt} \frac{\partial L}{\partial \dot{\mathbf{r}}} - \frac{\partial L}{\partial \mathbf{r}} - \boldsymbol{\tau} \right)^T \begin{pmatrix} \delta \mathbf{r} \\ \delta \zeta \end{pmatrix} = 0 \quad (80b)$$

$$\left(\frac{d}{dt} \frac{\partial L}{\partial \dot{\mathbf{r}}} - \frac{\partial L}{\partial \mathbf{r}} - \boldsymbol{\tau} \right) \delta \mathbf{r} + \left(\frac{d}{dt} \frac{\partial L}{\partial \dot{\zeta}} - \frac{\partial L}{\partial \zeta} \right) \delta \zeta = 0 \quad (80c)$$

$$GJ^{-T} \left(\frac{d}{dt} \frac{\partial L}{\partial \mathbf{r}} - \frac{\partial L}{\partial \mathbf{r}} - \boldsymbol{\tau} \right) \delta \zeta + \left(\frac{d}{dt} \frac{\partial L}{\partial \dot{\zeta}} - \frac{\partial L}{\partial \zeta} \right) \delta \zeta = 0 \quad (80d)$$

wherefore,

$$\left(\frac{d}{dt} \frac{\partial L}{\partial \dot{\zeta}} - \frac{\partial L}{\partial \zeta} \right) \delta \zeta + GJ^{-T} \left(\frac{d}{dt} \frac{\partial L}{\partial \mathbf{r}} - \frac{\partial L}{\partial \mathbf{r}} \right) = GJ^{-T} \boldsymbol{\tau} \quad (81)$$

given the arbitrariness of $\delta \zeta$. Equations (81) alongside (79) completely describe the system dynamics. Putting (63) into (81), we have

$$\left(\frac{d}{dt} \frac{\partial L}{\partial \dot{\zeta}} - \frac{\partial L}{\partial \zeta} \right) \delta \zeta = GJ^{-T} \left(1 - \frac{\rho}{2\|\mathbf{r}\|^2} \right) \boldsymbol{\tau}. \quad (82)$$

8 Results

Things to consider:

- (1) Try different linear solvers, direct and implicit solvers to compare simulation accuracy in SOFA

We now describe in detail the implementation of the kinematics and dynamics of the system we have been describing so far. We heavily rely on the SOFA simulation framework to realize our vision. We compose the scene graph of the head-IABs system as shown in ???. The patient is modeled as a rigid, in contact with the soft balls as shown in the figure body. In addition, we make the following definitions to simplify our problem abstractions.

Definition 1 (State). *The state of an object is a vector which contains all its degrees of freedom. For a mechanical system, this would include the position, velocity, acceleration, forces, and torques that inhibit or excite its motion along the constrained modes of deformation of the soft material.*

Definition 2 (Barycentric Coordinates). *For the deformation models of the soft robots, we introduce the barycentric coordinates [39], (t_1, t_2, t_3) , which are masses at the vertices of a triangle $\Delta T_1 T_2 T_3$ with which we discretize the deformable mesh of the solid object models.*

Definition 3 (Mappings). *The various geometric objects in the setup are hierarchically related to one another via a mapping mechanism. This mechanism propagates the forces and displacements that relate the several collisions, contacts, deformations, and displays and synchronizes them during simulation.*

In all our interactive simulations, we separate the mechanical finite element model from the collision and visual model in order to exploit distributed yet time-realistic evaluation of the various parts of our scene library. We apply a tetrahedron finite element model for discretizing each dome in the setup. We then project the edges of the uniform tetrahedron from its center on to the concentric unit sphere in order to obtain a network of arcs of great circles that decomposes the surface of the somes to spherical polygons, one for each face of the polyhedron.

For the domes that surround the head as shown in [Figure 5](#), we apply a volumetric mesh generation from the closed 3D surfaces of the closed STL files using a finite element modeling approach. At a facet angle of 10° , a circumferential radius of 1mm and a facet size of 0.1mm for the Delaunay balls, we generate 4,784 tetrahedrons for each dome. These are then used in carrying out the finite elastic deformation simulation model in SOFA. A barycentric mapping connects the deformable topologies of the dome heads with the carbon nanotube surface on which it rests.

9 Conclusions

We have presented the kinematic motion equations and the Lagrangian dynamics for the mechanism presented in our previous publication. It remains to demonstrate the working examples in closed-loop head motion control. In a follow-up paper to be released shortly, we show how these formulations are applied in real-time on the patient-IAB system.

A Deformation Gradient Derivation

It can be verified that the orthonormal basis vectors for [\(11\)](#) are

$$\begin{aligned} \mathbf{e}_r &= \frac{\partial \mathbf{r}}{\partial r} / \left| \frac{\partial \mathbf{r}}{\partial r} \right| = \begin{bmatrix} \cos \theta \sin \phi \\ \sin \theta \sin \phi \\ \cos \phi \end{bmatrix} & \mathbf{e}_\phi &= \frac{\partial \mathbf{r}}{\partial \phi} / \left| \frac{\partial \mathbf{r}}{\partial \phi} \right| = \begin{bmatrix} \cos \theta \cos \phi \\ \sin \theta \cos \phi \\ -\sin \phi \end{bmatrix} \\ \mathbf{e}_\theta &= \frac{\partial \mathbf{r}}{\partial \theta} / \left| \frac{\partial \mathbf{r}}{\partial \theta} \right| = \begin{bmatrix} -\sin \theta \\ \cos \theta \\ 0 \end{bmatrix}. \end{aligned} \quad (83)$$

From [\(14\)](#), we can write

$$\begin{aligned} \mathbf{F} &= \frac{\partial(\mathbf{dx}_r)}{\partial R} \mathbf{e}_r \otimes \mathbf{e}_R + \frac{1}{R} \frac{\partial}{\partial \Phi} (\mathbf{dx}_r \mathbf{e}_r) \otimes \mathbf{e}_\Phi + \frac{1}{R \sin \Phi} \frac{\partial(\mathbf{dx}_r \mathbf{e}_r)}{\partial \Theta} \otimes \mathbf{e}_\Theta \quad (84a) \\ &+ \frac{\partial}{\partial R} (\mathbf{dx}_\phi \mathbf{e}_\phi) \otimes \mathbf{e}_R + \frac{1}{R} \frac{\partial}{\partial \Phi} (\mathbf{dx}_\phi \mathbf{e}_\phi) \otimes \mathbf{e}_\Phi + \frac{1}{R \sin \Phi} \frac{\partial}{\partial \Theta} (\mathbf{dx}_\phi \mathbf{e}_\phi) \otimes \mathbf{e}_\Theta \\ &+ \frac{\partial}{\partial R} (\mathbf{dx}_\theta \mathbf{e}_\theta) \otimes \mathbf{e}_R + \frac{1}{R} \frac{\partial}{\partial \Phi} (\mathbf{dx}_\theta \mathbf{e}_\theta) \otimes \mathbf{e}_\Phi + \frac{1}{R \sin \Phi} \frac{\partial}{\partial \Theta} (\mathbf{dx}_\theta \mathbf{e}_\theta) \otimes \mathbf{e}_\Theta \end{aligned}$$

$$\begin{aligned}
\mathbf{F} = & \frac{\partial(\mathbf{dx}_r)}{\partial R} \mathbf{e}_r \otimes \mathbf{e}_R + \frac{1}{R \sin \Phi} \frac{\partial(\mathbf{dx}_r)}{\partial \Theta} \mathbf{e}_r \otimes \mathbf{e}_\Theta + \mathbf{dx}_r \frac{\sin \phi}{R \sin \Phi} \mathbf{e}_\theta \otimes \mathbf{e}_\Theta \\
& + \frac{\mathbf{dx}_r}{R} \mathbf{e}_\phi \otimes \mathbf{e}_\Phi + \frac{1}{R} \frac{\partial(\mathbf{dx}_r)}{\partial \Phi} \mathbf{e}_r \otimes \mathbf{e}_\Phi + \frac{\partial(\mathbf{dx}_\phi)}{\partial R} \mathbf{e}_\phi \otimes \mathbf{e}_R + 0 - \frac{\mathbf{dx}_\phi}{R} \mathbf{e}_r \otimes \mathbf{e}_\Phi \\
& + \frac{1}{R} \frac{\partial(\mathbf{dx}_\phi)}{\partial \Phi} \mathbf{e}_\phi \otimes \mathbf{e}_\Phi + \cos \phi \frac{\mathbf{dx}_\phi}{R \sin \Phi} \mathbf{e}_\theta \otimes \mathbf{e}_\Theta + \frac{1}{R \sin \Phi} \frac{\partial(\mathbf{dx}_\phi)}{\partial \Theta} \mathbf{e}_\phi \otimes \mathbf{e}_\Theta \\
& + \frac{\partial(\mathbf{dx}_\theta)}{\partial R} \mathbf{e}_\theta \otimes \mathbf{e}_R + 0 + \frac{1}{R} \frac{\partial(\mathbf{dx}_\theta)}{\partial \Phi} \mathbf{e}_\theta \otimes \mathbf{e}_\Phi + 0 + \frac{1}{R \sin \Phi} \frac{\partial(\mathbf{dx}_\theta)}{\partial \Theta} \mathbf{e}_\theta \otimes \mathbf{e}_\Theta \\
& + \frac{\mathbf{dx}_\theta}{R \sin \Phi} (-\mathbf{e}_r \sin \phi - \mathbf{e}_\phi \cos \phi) \otimes \mathbf{e}_\Theta
\end{aligned} \tag{84b}$$

where we have made use of the chain rule, (12), together with the identities,

$$\frac{\partial \mathbf{e}_r}{\partial r} = \frac{\partial \mathbf{e}_\phi}{\partial r} = \frac{\partial \mathbf{e}_\theta}{\partial r} = \frac{\partial \mathbf{e}_\theta}{\partial \phi} = 0 \quad \frac{\partial \mathbf{e}_\phi}{\partial \phi} = -\mathbf{e}_r \quad \frac{\partial \mathbf{e}_r}{\partial \phi} = \mathbf{e}_\phi \tag{85a}$$

$$\frac{\partial \mathbf{e}_r}{\partial \theta} = \mathbf{e}_\theta \sin \phi \quad \frac{\partial \mathbf{e}_\phi}{\partial \theta} = \mathbf{e}_\theta \cos \phi \quad \frac{\partial \mathbf{e}_\theta}{\partial \theta} = -(\mathbf{e}_r \sin \phi + \mathbf{e}_\phi \cos \phi) \tag{85b}$$

in carrying out the partial derivatives of (84). In matrix form, we rewrite (84) as

$$\mathbf{F} = \left(\begin{array}{ccc} \frac{\partial(\mathbf{dx}_r)}{\partial R} & \frac{\partial(\mathbf{dx}_r)}{R \partial \Phi} - \frac{\mathbf{dx}_\phi}{R} & \frac{1}{R \sin \Phi} \frac{\partial(\mathbf{dx}_r)}{\partial \Theta} - \frac{\sin \phi}{R \sin \Phi} \mathbf{dx}_\theta \\ \frac{\partial(\mathbf{dx}_\phi)}{\partial R} & \frac{\mathbf{dx}_r}{R} + \frac{1}{R} \frac{\partial(\mathbf{dx}_\phi)}{\partial \Phi} & \frac{1}{R \sin \Phi} \frac{\partial(\mathbf{dx}_\phi)}{\partial \Theta} - \frac{\cos \phi}{R \sin \Phi} \mathbf{dx}_\theta \\ \frac{\partial(\mathbf{dx}_\theta)}{\partial R} & \frac{1}{r} \frac{\partial \mathbf{dx}_\theta}{\partial \phi} & \frac{1}{R \sin \Phi} \left(\frac{\partial(\mathbf{dx}_\theta)}{\partial \Theta} + \cos \phi \mathbf{dx}_\phi + \sin \phi \mathbf{dx}_r \right) \end{array} \right) \tag{86a}$$

which as a result of the local volume preservation principle *i.e.* (12), becomes

$$\mathbf{F} = \left(\begin{array}{ccc} \frac{\partial(\mathbf{dx}_r)}{\partial R} & \frac{\partial(\mathbf{dx}_r)}{R \partial \Phi} - \frac{\mathbf{dx}_\phi}{R} & \frac{1}{R \sin \Phi} \frac{\partial(\mathbf{dx}_r)}{\partial \Theta} - \frac{\mathbf{dx}_\theta}{R} \\ \frac{\partial(\mathbf{dx}_\phi)}{\partial R} & \frac{\mathbf{dx}_r}{R} + \frac{1}{R} \frac{\partial(\mathbf{dx}_\phi)}{\partial \Phi} & \frac{1}{R \sin \Phi} \frac{\partial(\mathbf{dx}_\phi)}{\partial \Theta} - \cot \phi \frac{\mathbf{dx}_\theta}{R} \\ \frac{\partial(\mathbf{dx}_\theta)}{\partial R} & \frac{1}{r} \frac{\partial \mathbf{dx}_\theta}{\partial \phi} & \frac{\mathbf{dx}_\phi}{R} \cot \phi + \frac{\mathbf{dx}_r}{R} + \frac{1}{R \sin \Phi} \frac{\partial(\mathbf{dx}_\theta)}{\partial \Theta} \end{array} \right) \tag{87}$$

or

$$\mathbf{F} = \left(\begin{array}{ccc} \frac{R^2}{r^2} & -\frac{\phi}{R} & -\frac{\theta}{R} \\ 0 & \frac{r}{R} + \frac{1}{R} & -\frac{\theta}{R} \cot \phi \\ 0 & 0 & \frac{r}{R} + \frac{\phi}{R} \cot \phi + \frac{1}{R \sin \Phi} \end{array} \right). \tag{88}$$

B Robot-Head Dynamics

We now derive the overall dynamics for the elastic IAB in Eulerian form. Following (33), a point on the surface of the IAB has the following description

$$\mathbf{r} = \begin{bmatrix} \lambda \\ r \\ \phi \end{bmatrix} = \begin{bmatrix} r/R \\ (R_\circ^3 + r_i^3 - R_i^3)^{1/3} \\ \beta - \alpha \end{bmatrix} \quad (89)$$

so that the Eulerian time differentiation of \mathbf{r} yields

$$\dot{\mathbf{r}} = [\dot{\lambda}, \dot{r}, \dot{\phi}]^T = [\dot{r}/R, 3r_i^2\dot{r}_i, -\dot{\alpha}]^T \quad (90)$$

which follows since $\dot{R} = \dot{\beta} = 0$ in the reference configuration. Similarly, we find that $\ddot{\mathbf{r}}$ is given as

$$\ddot{\mathbf{r}} = [\ddot{\lambda}, \ddot{r}, \ddot{\phi}]^T = [\ddot{r}/R, 6r_i\dot{r}_i^2 + 3r_i\ddot{r}_i, -\ddot{\alpha}]^T \quad (91)$$

Recall the kinetic energy form of a continuum body (§ 5)

$$T = \frac{1}{2}\rho\mathbf{v}(\mathbf{r}, t) \cdot \mathbf{v}(\mathbf{r}, t) = \frac{1}{2}\rho\|\dot{\mathbf{r}}\|^2. \quad (92)$$

Given the incompressibility of the IAB material body, the material mass density is uniform throughout the body at a configuration so that the rate of change of the body mass, ρ , vanishes.

B.1 Case I: Cauchy Elastic IAB Material Skins

Suppose we choose a Cauchy Elastic material so that the constitutive equation that governs the Cauchy stress tensor, σ , is independent of the path of the deformation from the reference configuration but is solely a function of the state of deformation. Then, it follows that $V = 0$. We have

$$T = \frac{1}{2}\rho\|\dot{\mathbf{r}}\|^2 = \frac{1}{2}\rho(\dot{r}^2/R^2 + 9r_i^4\dot{r}_i^2 + \dot{\alpha}^2), \quad V = 0. \quad (93)$$

It follows that the Lagrangian is

$$L(\mathbf{r}, \dot{\mathbf{r}}) = \frac{1}{2}\rho\|\dot{\mathbf{r}}\|^2 = \frac{1}{2}\rho(\dot{r}^2/R^2 + 9r_i^4\dot{r}_i^2 + \dot{\alpha}^2) \quad (94)$$

and the derivatives of the canonical momenta are

$$\frac{d}{dt} \frac{\partial L}{\partial \dot{r}} = \frac{d}{dt} \left(\frac{\rho \dot{r}}{R^2} \right) = \rho \left(\frac{\ddot{r}}{R^2} - 2 \frac{\dot{r} \dot{R}}{R^3} \right) \equiv \frac{\rho}{R^2} \ddot{r} \quad (95a)$$

$$\frac{d}{dt} \frac{\partial L}{\partial \dot{r}_i} = \frac{d}{dt} (9\rho r_i^4 \dot{r}_i) = 9\rho r_i^3 (4\dot{r}_i^2 + r_i \ddot{r}_i) \quad (95b)$$

$$\frac{d}{dt} \frac{\partial L}{\partial \dot{\alpha}} = \frac{d}{dt} \frac{\partial L}{\partial \dot{\alpha}} = \frac{d}{dt} (\rho \dot{\alpha}) = \rho \ddot{\alpha}, \quad (95c)$$

where (95a) follows from the fact that the radius is constant in the reference configuration. We therefore have the following associated generalized forces

$$\frac{\partial L}{\partial r} = 0, \frac{\partial L}{\partial R} = -\frac{\rho \dot{r}^2}{R^3} \text{ and } \frac{\partial L}{\partial \phi} = 0. \quad (96a)$$

Recalling the Euler-Lagrange equation from (56), we may write the torque that governs the j 'th IAB as (we have dropped the j 'th index)

Cauchy-Elastic IAB Material Torque

$$\boldsymbol{\tau} = \frac{\rho \ddot{r}}{R^2} + 9\rho r_i^4 \ddot{r}_i + \rho \ddot{\alpha} + \frac{\rho \dot{r}^2}{R^3} + 36\rho r_i^3 \dot{r}_i^2 \quad (97)$$

and in matrix form for all the system of IABs, we have

$$\begin{aligned} \boldsymbol{\tau} &= \begin{bmatrix} \rho/R^2 & 0 & 0 \\ 0 & 9\rho r_i^4/2 & 0 \\ 0 & 0 & \rho \end{bmatrix} \begin{bmatrix} \ddot{r} \\ \ddot{r}_i \\ \ddot{\alpha} \end{bmatrix} \\ &+ \begin{bmatrix} \dot{r} \\ \dot{r}_i \\ \dot{\alpha} \end{bmatrix}^T \begin{bmatrix} \rho/R^3 & 0 & 0 \\ 0 & 36\rho r_i^3 & 0 \\ 0 & 0 & 0 \end{bmatrix} \begin{bmatrix} \dot{r} \\ \dot{r}_i \\ \dot{\alpha} \end{bmatrix} \end{aligned} \quad (98)$$

rewritten compactly as,

$$\boldsymbol{\tau} = \underbrace{\begin{bmatrix} \rho/R^2 & 0 & 0 \\ 0 & 9\rho r_i^4/2 & 0 \\ 0 & 0 & \rho \end{bmatrix}}_{M_{iab}} \ddot{\mathbf{r}} + \underbrace{\begin{bmatrix} \rho/R^3 \dot{r} & 0 & 0 \\ 0 & 36\rho r_i^3 \dot{r}_i & 0 \\ 0 & 0 & 0 \end{bmatrix}}_{C_{iab}} \dot{\mathbf{r}} \quad (99)$$

or

$$\boldsymbol{\tau} = M_{iab}(\mathbf{r}) \ddot{\mathbf{r}} + C_{iab}(\mathbf{r}, \dot{\mathbf{r}}) \dot{\mathbf{r}} \quad (100)$$

B.2 Case II: Green Elastic IAB Material Skins

When the stress tensor depends on the strain, we have from (67), that

$$V(\mathbf{r}) = \mathbf{tr}(\mathbf{S}\dot{\mathbf{F}}). \quad (101)$$

The associated force on the head is now a function of the kinetic and potential energies so that we have

$$L(\mathbf{r}, \dot{\mathbf{r}}) = \frac{1}{2} \rho \|\dot{\mathbf{r}}\|^2 + \mathbf{tr}(\mathbf{S}\dot{\mathbf{F}}) \quad (102a)$$

$$= \frac{1}{2} \rho (\dot{r}^2/R^2 + 9r_i^4 \dot{r}_i^2 + \dot{\alpha}^2) + \mathbf{tr}(\mathbf{S}\dot{\mathbf{F}}) \quad (102b)$$

$$= \frac{1}{2} \rho (\dot{r}^2/R^2 + 9r_i^4 \dot{r}_i^2 + \dot{\alpha}^2) + \mathbf{tr}(J \mathbf{H}^T \boldsymbol{\sigma} \dot{\mathbf{F}})$$

which follows from (39). We thus have

$$L(\mathbf{r}, \dot{\mathbf{r}}) = \frac{1}{2} \rho (\dot{r}^2/R^2 + 9r_i^4 \dot{r}_i^2 + \dot{\alpha}^2) + \mathbf{tr}(\mathbf{F}^{-1} \boldsymbol{\sigma} \dot{\mathbf{F}}) \quad (103)$$

Recall from [22] that

$$\mathbf{F} = \begin{bmatrix} \frac{R^2}{r^2} & 0 & 0 \\ 0 & \frac{r}{R} & 0 \\ 0 & 0 & \frac{r}{R} \end{bmatrix} \text{ and } \boldsymbol{\sigma} = C_1 \mathbf{B} - C_2 \mathbf{C}^{-1} - p \mathbf{I} \quad (104)$$

where C_1 and C_2 are appropriate IAB material moduli, p is the hydrostatic pressure and \mathbf{B} , \mathbf{C} respectively denote the left and right Cauchy-Green deformation tensors. We therefore have the following for the Green-Elastic IAB material Lagrangian

$$L(\mathbf{r}, \dot{\mathbf{r}}) = \frac{1}{2} \rho (\dot{r}^2/R^2 + 9r_i^4 \dot{r}_i^2 + \dot{\alpha}^2) + \mathbf{tr}(\mathbf{F}^{-1} \boldsymbol{\sigma} \dot{\mathbf{F}}) \quad (105)$$

$$\begin{aligned} &= \frac{1}{2} \rho (\dot{r}^2/R^2 + 9r_i^4 \dot{r}_i^2 + \dot{\alpha}^2) \\ &\quad + 2C_1 \left(\frac{R^3}{r^4} - \frac{r^2}{R^3} \right) + 2C_2 \left(\frac{R}{r^2} - \frac{r^4}{R^5} \right) \end{aligned} \quad (106)$$

where we have taken $\dot{\mathbf{F}}$ is the time derivative of \mathbf{F} with respect to r . Solving for the derivatives of the kinetic and potential energy as before, we have,

$$\frac{d}{dt} \frac{\partial L}{\partial \ddot{r}} = \frac{\rho}{R^2} \ddot{r}, \quad \frac{d}{dt} \frac{\partial L}{\partial \ddot{r}_i} = 9\rho r_i^3 (4\dot{r}_i^2 + r_i \ddot{r}_i) \quad (107a)$$

$$\frac{d}{dt} \frac{\partial L}{\partial \dot{\phi}} = \rho \ddot{\alpha} \quad (107b)$$

with the following associated generalized forces

$$\frac{\partial L}{\partial r} = -4C_2 \left(\frac{2r^3}{R^5} - \frac{R}{r^3} \right) - 4C_1 \left(\frac{2R^3}{r^5} - \frac{r}{R^3} \right), \quad (108a)$$

$$\frac{\partial L}{\partial r_i} = 18r_i^3 \dot{r}_i^2 \text{ and } \frac{\partial L}{\partial \phi} = 0. \quad (108b)$$

We can now write the torque as

Green-Elastic IAB Material Torque

$$\begin{aligned} \boldsymbol{\tau} &= \frac{\rho \ddot{r}}{R^2} + 9\rho r_i^4 \ddot{r}_i + \rho \ddot{\alpha} + \frac{\rho \dot{r}^2}{R^3} + 36\rho r_i^3 \dot{r}_i^2 \\ &\quad + 4C_1 \left(\frac{2R^3}{r^5} + \frac{r}{R^3} \right) + 4C_2 \left(\frac{2r^3}{R^5} + \frac{R}{r^3} \right) \end{aligned} \quad (109)$$

C Derivation of IAB-Head Contact Kinematics

Here, we formulate the contact kinematics between an IAB and the head in a fashion similar to the single finger soft contact type postulated in [17]. We note that an alternative derivation that is more concise can be found in [15].

C.1 Contact Coordinates and Gaussian Map

Following equations (46a), (46b), and 47, we write

$$R f_1(\alpha_1) + p = f_h(\alpha_h) \quad (110a)$$

$$R n_1(\alpha_1) = -n_h(\alpha_h) \quad (110b)$$

$$R \frac{\partial f_1}{\partial \alpha_1} M_1^{-1} R_\psi = \frac{\partial f_h}{\partial \alpha_h} M_h^{-1}. \quad (110c)$$

Differentiating (110a) and (110b), we find that

$$\dot{R} f_1(\alpha_1) + R \frac{\partial f_1}{\partial \alpha_1} \dot{\alpha}_1 + \dot{p} = \frac{\partial f_h}{\partial \alpha_h} \dot{\alpha}_h \quad (111)$$

$$\dot{R} n_1(\alpha_1) + R \frac{\partial n_1}{\partial \alpha_1} \dot{\alpha}_1 = -\frac{\partial n_h}{\partial \alpha_h} \dot{\alpha}_h. \quad (112)$$

It follows through the multiplication of (111) by $\frac{\partial f_h}{\partial \alpha_h}^T$ and putting α_h into (112), we have

$$\begin{aligned} \dot{R} n_1(\alpha_1) + R \frac{\partial n_1}{\partial \alpha_1} \dot{\alpha}_1 &= -\frac{\partial n_h}{\partial \alpha_h} M_h^{-2} \frac{\partial f_h}{\partial \alpha_h}^T \\ &\quad \left(\dot{R} f_1(\alpha_1) + R \frac{\partial f_1}{\partial \alpha_1} \dot{\alpha}_1 + \dot{p} \right). \end{aligned} \quad (113)$$

Now, putting (110c) into (113) and rearranging, we find that

$$\begin{aligned} &\left[R \frac{\partial n_1}{\partial \alpha_1} + \frac{\partial n_h}{\partial \alpha_h} M_h^{-2} \left(\frac{\partial f_h^T}{\partial \alpha_h} \frac{\partial f_h}{\partial \alpha_h} \right) M_h^{-1} R_\psi M_1 \right] \dot{\alpha}_1 \\ &= -\dot{R} n_1 - \frac{\partial n_h}{\partial \alpha_h} M_h^{-2} \frac{\partial f_h}{\partial \alpha_h}^T \left(\dot{R} f_1(\alpha_1) + \dot{p} \right). \end{aligned} \quad (114)$$

Multiplying throughout by $M_h^{-T} \frac{\partial f_h}{\partial \alpha_h}^T$, we have on the left hand side of the above as,

$$M_h^{-T} \frac{\partial f_h}{\partial \alpha_h}^T \left(R \frac{\partial n_1}{\partial \alpha_1} + \frac{\partial n_h}{\partial \alpha_h} M_h^{-1} R_\psi M_1 \right) \dot{\alpha}_1. \quad (115)$$

Since

$$\begin{aligned} M_h^{-T} \frac{\partial f_h}{\partial \alpha_h}^T &= \frac{\partial f_h}{\partial \alpha_h} M_h^{-1} = \left(R \frac{\partial f_1}{\partial \alpha_1} M_1^{-1} R_\psi \right)^T \\ &= R_\psi M_1^{-T} \frac{\partial f_1}{\partial \alpha_1}^T R^T, \end{aligned} \quad (116)$$

equation (115) becomes

$$\begin{aligned} \dot{\alpha}_1 & \left(R_\psi M_1^{-T} \frac{\partial f_1}{\partial \alpha_1}^T \frac{\partial n_1}{\partial \alpha_1} + M_h^{-T} \frac{\partial f_h}{\partial \alpha_h}^T \frac{\partial n_h}{\partial \alpha_h} M_h^{-1} R_\psi M_1 \right) \\ & = \left(R_\psi M_1^{-T} \frac{\partial f_1}{\partial \alpha_1}^T \frac{\partial n_1}{\partial \alpha_1} M_1^{-1} R_\psi + M_h^{-T} \frac{\partial f_h}{\partial \alpha_h}^T \frac{\partial n_h}{\partial \alpha_h} M_h^{-1} \right) \\ & \quad \times R_\psi M_1 \dot{\alpha}_1. \end{aligned} \quad (117)$$

Setting

$$\tilde{\mathcal{K}}_1 = R_\psi M_1^{-T} \frac{\partial f_1}{\partial \alpha_1}^T \frac{\partial n_1}{\partial \alpha_1} M_1^{-1} R_\psi$$

and

$$\mathcal{K}_h = M_h^{-T} \frac{\partial f_h}{\partial \alpha_h}^T \frac{\partial n_h}{\partial \alpha_h} M_h^{-1},$$

it follows from (113) that

$$\begin{aligned} (\tilde{\mathcal{K}}_1 + \mathcal{K}_h) R_\psi M_1 \dot{\alpha}_1 & = \\ M_h^{-T} \frac{\partial f_h}{\partial \alpha_h}^T & \left[-\dot{R} n_1 - \frac{\partial n_h}{\partial \alpha_h} M_h^{-2} \frac{\partial f_h}{\partial \alpha_h}^T (\dot{R} f_1 + \dot{p}) \right] \\ & = -M_h^{-T} \frac{\partial f_h}{\partial \alpha_h}^T \dot{R} n_1 - \mathcal{K}_h M_h^{-T} \frac{\partial f_h}{\partial \alpha_h}^T (\dot{R} f_1 + \dot{p}) \end{aligned} \quad (118)$$

so that

$$\begin{aligned} \dot{\alpha}_1 & = (\tilde{\mathcal{K}}_1 + \mathcal{K}_h)^{-1} R_\psi M_1^{-1} \times \\ & \underbrace{-M_h^{-T} \frac{\partial f_h}{\partial \alpha_h}^T \dot{R} n_1}_{w_t} \underbrace{-\mathcal{K}_h M_h^{-T} \frac{\partial f_h}{\partial \alpha_h}^T (\dot{R} f_1 + \dot{p})}_{v_t} \end{aligned} \quad (119)$$

or

$$\dot{\alpha}_1 = (\tilde{\mathcal{K}}_1 + \mathcal{K}_h)^{-1} R_\psi M_1^{-1} (w_t - \mathcal{K}_h v_t). \quad (120)$$

Finding the generalized velocity of the head with respect to a single IAB deformation is tantamount to finding $(\hat{w}, v) = \dot{g} g^{-1}$. Thus,

$$\omega_t = -M_h^{-T} \frac{\partial f_h}{\partial \alpha_h}^T (\omega \times (R n_1)) = -M_h^{-T} \frac{\partial f_h}{\partial \alpha_h}^T (n_h \times \omega) \quad (121)$$

$$v_t = M_h^{-T} \frac{\partial f_h}{\partial \alpha_h}^T (\omega \times (R f_1) + \omega \times p + v) \quad (122)$$

$$= M_h^{-T} \frac{\partial f_h}{\partial \alpha_h}^T (-f_h \times \omega + v), \quad (123)$$

where ω_t is the head's rolling velocity projected onto the contact's tangent plane. The rotation normal to the surface is canceled by the cross product of ω and n_h . In the same vein, v_t is the sliding velocity between the contacts, projected onto the tangent plane. Following the above construction, we find the kinematics of the contact point of the head in local coordinates is

$$\dot{\alpha}_h = M_h^{-1} \left(\tilde{\mathcal{K}}_1 + \mathcal{K}_h \right)^{-1} (\omega_t - \tilde{\mathcal{K}}_1 v_t), \quad (124)$$

where $(\tilde{\mathcal{K}}_1 + \mathcal{K}_h)$ is the *relative curvature* [15]. It remains to solve for the relative orientation between the two local coordinates, ψ .

C.2 Relative Contact Orientation and Torsion Metric Tensors

In matrix form, (110b) and (110c) can be written as,

$$R \begin{bmatrix} \frac{\partial f_1}{\partial \alpha_1} M_1^{-1} & n_1(\alpha_1) \end{bmatrix} \begin{bmatrix} R_\psi & 0 \\ 0 & -1 \end{bmatrix} = \begin{bmatrix} \frac{\partial f_h}{\partial \alpha_h} M_h^{-1} & n_h(\alpha_h) \end{bmatrix}. \quad (125)$$

Following the normalized Gaussian frame defined in (50), we can rewrite the above equation as

$$R[x_1 \ y_1 \ z_1] \bar{R}_\psi = [x_h \ y_h \ z_h]. \quad (126)$$

The total derivative of (126) yields

$$\begin{aligned} & \dot{R}[x_1 \ y_1 \ z_1] \bar{R}_\psi + R[\dot{x}_1 \ \dot{y}_1 \ \dot{z}_1] \bar{R}_\psi + \\ & R[x_1 \ y_1 \ z_1] \begin{bmatrix} \dot{R}_\psi & 0 \\ 0 & 0 \end{bmatrix} = \begin{bmatrix} \dot{x}_h \\ \dot{y}_h \\ \dot{z}_h \end{bmatrix}^T. \end{aligned} \quad (127)$$

Premultiplying by $y_1^T R^T$ and then postmultiplying by $\bar{R}_\psi \begin{pmatrix} 1 \\ 0 \\ 0 \end{pmatrix}$, with the knowledge that $\bar{R}_\psi \bar{R}_\psi = \mathbf{I}$, and the identity $y_1^T y_1 = 1$, we find that

$$\begin{aligned} & y_1^T R^T \dot{R} [x_1 \ y_1 \ z_1] \bar{R}_\psi + y_1^T [\dot{x}_1, \ \dot{y}_1, \ \dot{z}_1] \bar{R}_\psi \\ & + (0 \ 1 \ 0) \begin{bmatrix} \dot{R}_\psi & 0 \\ 0 & 0 \end{bmatrix} = y_1^T R^T [\dot{x}_h \ \dot{y}_h \ \dot{z}_h] \end{aligned} \quad (128)$$

$$\begin{aligned} & y_1^T R^T \dot{R} x_1 + y_1^T \dot{x}_1 + (0 \ 1 \ 0) \begin{bmatrix} \dot{R}_\psi & R_\psi & 0 \\ 0 & 0 & 0 \end{bmatrix} \begin{pmatrix} 1 \\ 0 \\ 0 \end{pmatrix} \\ & = y_1^T R^T [\dot{x}_h \ \dot{y}_h \ \dot{z}_h] \bar{R}_\psi \begin{pmatrix} 1 \\ 0 \\ 0 \end{pmatrix} \end{aligned} \quad (129)$$

$$\begin{aligned} & y_1^T R^T \dot{R} x_1 + y_1^T \dot{x}_1 + (0 \ -1) \begin{bmatrix} 0 & \dot{\psi} \\ -\dot{\psi} & 0 \end{bmatrix} \begin{pmatrix} 1 \\ 0 \end{pmatrix} \\ & = y_1^T R^T [\dot{x}_h \ \dot{y}_h \ \dot{z}_h] \bar{R}_\psi \begin{pmatrix} 1 \\ 0 \\ 0 \end{pmatrix} \end{aligned} \quad (130)$$

$$y_1^T R^T \dot{R} x_1 + y_1^T \dot{x}_1 - \dot{\psi} = y_1^T R^T [\dot{x}_h \ \dot{y}_h \ \dot{z}_h] \bar{R}_\psi \begin{pmatrix} 1 \\ 0 \\ 0 \end{pmatrix}. \quad (131)$$

From (126), we have that

$$\bar{R}_\psi^T [x_1^T \ y_1^T \ z_1^T] R^T = [x_h^T \ y_h^T \ z_h^T] \quad (132)$$

so that

$$[x_1^T \ y_1^T \ z_1^T] R^T = \bar{R}_\psi [x_h^T \ y_h^T \ z_h^T] \quad (133)$$

or

$$\begin{aligned} y_1^T R^T &= (0 \ 1 \ 0) \bar{R}_\psi [x_h^T \ y_h^T \ z_h^T] \\ &= (0 \ 1) R_\psi \begin{pmatrix} x_h^T \\ y_h^T \end{pmatrix}. \end{aligned} \quad (134)$$

It follows from (131) that

$$\begin{aligned} \dot{\psi} &= y_1^T R^T \dot{R} x_1 + y_1^T \frac{\partial x_1}{\partial \alpha_1} \dot{\alpha}_1 \\ &\quad - (0, 1) R_\psi \begin{bmatrix} x_h^T \dot{x}_h & x_h^T \dot{y}_h \\ y_h^T \dot{x}_h & y_h^T \dot{y}_h \end{bmatrix} R_\psi \begin{pmatrix} 1 \\ 0 \end{pmatrix}. \end{aligned} \quad (135)$$

Using the identities,

$$x_i^T y_i = 0, \implies \dot{x}_i^T y_i = -x_i^T \dot{y}_i = y_i^T \dot{x}_i \quad (136)$$

$$x_i^T x_i = 1, \implies \dot{x}_i^T x_i = 0, \quad (137)$$

we can rewrite (135) as

$$\begin{aligned}\dot{\psi} &= y_1^T R^T \dot{R} x_1 + y_h^T \frac{\partial x_h}{\partial \alpha_h} \dot{\alpha}_h + y_1^T \frac{\partial x_1}{\partial \alpha_1} \dot{\alpha}_1 \\ &= \omega_n + T_h M_h \dot{\alpha}_h + T_1 M_1 \dot{\alpha}_1\end{aligned}\quad (138)$$

where

$$\begin{aligned}\omega_n &= y_1^T R^T \dot{R} x_1 = (R y_1)^T w \times (R x_1) \\ &= (R z_1)^T \omega = z_h^T \omega\end{aligned}\quad (139)$$

$$T_h = y_h \frac{\partial x_h^T}{\partial \alpha_h} M_h^{-T}, \quad T_1 = y_1 \frac{\partial x_1^T}{\partial \alpha_1} M_1^{-T}. \quad (140)$$

It follows that the first, second and third equations of contact are given by (120), (124), and (138) respectively, *i.e.*

Equations of Contact

$$\dot{\alpha}_1 = \left(\tilde{\mathcal{K}}_1 + \mathcal{K}_h \right)^{-1} R_\psi M_1^{-1} (\omega_t - \mathcal{K}_h v_t) \quad (141a)$$

$$\dot{\alpha}_h = M_h^{-1} \left(\tilde{\mathcal{K}}_1 + \mathcal{K}_h \right)^{-1} (\omega_t - \tilde{\mathcal{K}}_1 v_t) \quad (141b)$$

$$\dot{\psi} = \omega_n + T_h M_h \dot{\alpha}_h + T_1 M_1 \dot{\alpha}_1. \quad (141c)$$

References

1. Allen, J.J., Mäthger, L.M., Barbosa, A., Hanlon, R.T.: Cuttlefish use visual cues to control three-dimensional skin papillae for camouflage. *Journal of Comparative Physiology A* **195**(6), 547–555 (2009) [3](#)
2. Chen, R.T.Q., Rubanova, Y., Bettencourt, J., Duvenaud, D.: Neural ordinary differential equations. *Advances in Neural Information Processing Systems* (2018)
3. Clauser, C.E., McConville, J.T., Young, J.W.: Weight, volume, and center of mass of segments of the human body. Tech. rep., Antioch Coll Yellow Springs OH (1969) [5](#)
4. Donlon, E., Dong, S., Liu, M., Li, J., Adelson, E., Rodriguez, A.: Gelslim: A high-resolution, compact, robust, and calibrated tactile-sensing finger. In: 2018 IEEE/RSJ International Conference on Intelligent Robots and Systems (IROS), pp. 1927–1934. IEEE (2018) [3](#)
5. Fung, Y., Tong, P., Chen, X.: Classical and computational solid mechanics, vol. 2. World Scientific Publishing Company (2001) [12](#)
6. George Thuruthel, T., Ansari, Y., Falotico, E., Laschi, C.: Control Strategies for Soft Robotic Manipulators: A Survey. *Soft Robotics* **5**(2), 149–163 (2018). DOI 10.1089/soro.2017.0007 [1, 2](#)
7. Hanlon, R.T., Messenger, J.B.: Adaptive coloration in young cuttlefish (*sepia officinalis* l.): the morphology and development of body patterns and their relation to behaviour. *Philosophical Transactions of the Royal Society of London. B, Biological Sciences* **320**(1200), 437–487 (1988) [3](#)

8. Hannan, M.W., Walker, I.D.: Novel Kinematics for Continuum Robots. pp. 227–238. Advances in Robot Kinematics (2000) [2](#)
9. Hannan, M.W., Walker, I.D.: Kinematics and the Implementation of an Elephant’s Trunk Manipulator and Other Continuum Style Robots. Journal of Robotic Systems **20**(2), 45–63 (2003) [2](#)
10. Holzapfel, G.A., Gasser, T.C., Ogden, R.W.: A new constitutive framework for arterial wall mechanics and a comparative study of material models. Journal of elasticity and the physical science of solids **61**(1-3), 1–48 (2000) [11](#)
11. Hunt, K.H.: Kinematic Geometry of Mechanisms. Oxford University Press (1977) [2](#), [6](#)
12. Jones, B.A., Walker, I.D.: Kinematics for Multisection Continuum Robots.pdf **22**(1), 43–55 (2006) [2](#)
13. Kapadia, A.D., Fry, K.E., Walker, I.D.: Empirical investigation of closed-loop control of extensible continuum manipulators. In: 2014 IEEE/RSJ International Conference on Intelligent Robots and Systems, pp. 329–335. IEEE (2014) [2](#)
14. Kerr, J.R.: An Analysis of Multi-Fingered Hands. International Journal of Robotics Research (Dept. of Mechanical Engineering), 3–17 (1984) [24](#)
15. Montana, D.J.: The Kinematics of Contact And Grasp. The International Journal of Robotics Research **7**(3), 17–32 (1988) [16](#), [20](#), [32](#), [34](#)
16. Mooney, M.: A theory of large elastic deformation. Journal of applied physics **11**(9), 582–592 (1940) [2](#), [8](#)
17. Murray, R.M., Sastry, S.: Grasping and Manipulation using Multifingered Robot Hands. In: Proceedings of Symposia in Applied Mathematics, vol. 41, pp. 329–335 (1990) [19](#), [32](#)
18. Nguyen, V.D.: Constructing force-closure grasps. The International Journal of Robotics Research **7**(3), 3–16 (1988) [15](#)
19. Ogden, R.: Non-linear Elastic Deformations. Dover Publicationsbs, Inc., Mineola, New York (1997) [2](#), [7](#), [11](#), [14](#), [16](#), [22](#)
20. Ogunmolu, O., Gans, N., Jiang, S., Gu, X.: An Image Guided Soft Robotic Patient Positioning System for Maskless Head And Neck Cancer Radiotherapy: A Proof of Concept Study. Medical Physics: The International Journal of Medical Physics Research and Practice **42**, 3266–3266 (2015) [1](#)
21. Ogunmolu, O., Kulkarni, A., Tadesse, Y., Gu, X., Jiang, S., Gans, N.: Soft-neuroadapt: A 3-dof neuro-adaptive patient pose correction system for frameless and maskless cancer radiotherapy. In: IEEE/RSJ International Conference on Intelligent Robots and Systems (IROS), Vancouver, BC, CA, pp. 3661–3668. IEEE (2017) [2](#)
22. Ogunmolu, O., Liu, X., Gans, N., Wiersma, R.: Mechanism and Constitutive Model of a Continuum Robot for Head and Neck Cancer Radiotherapy. In: IEEE International Conference on Robotics and Automation (ICRA), Paris, France (2020) [13](#), [14](#), [15](#), [16](#), [17](#), [23](#), [31](#)
23. Ogunmolu, O., Wiersma, R.D.: Towards Real-Time Motion Compensation in Radio-Transparent Robotic Radiation Therapy. [2](#)
24. Ogunmolu, O.P.: A Multi-DOF Soft Robot Mechanism for Patient Motion Correction and Beam Orientation Selection in Cancer Radiation Therapy. Ph.D. thesis, The University of Texas at Dallas; UT Southwestern Medical Center (2019) [2](#), [7](#), [14](#)
25. Ogunmolu, O.P., Gu, X., Jiang, S., Gans, N.R.: A real-time, soft robotic patient positioning system for maskless head-and-neck cancer radiotherapy: An initial investigation. In: Automation Science and Engineering (CASE), 2015 IEEE International Conference on, Gothenburg, Sweden, pp. 1539–1545. IEEE (2015) [1](#)
26. Ogunmolu, O.P., Gu, X., Jiang, S., Gans, N.R.: Vision-based control of a soft robot for maskless head and neck cancer radiotherapy. In: Automation Science and Engineering (CASE), 2016 IEEE International Conference on, Fort Worth, Texas, pp. 180–187. IEEE (2016) [2](#)

27. Pikul, J., Cohen, I., Shepherd, R.: Stretchable surfaces with programmable texture (2019). US Patent App. 16/161,029 [2](#), [3](#)
28. Pikul, J.H., Li, S., Bai, H., Hanlon, R.T., Cohen, I., Shepherd, R.F.: Stretchable surfaces with programmable 3d texture morphing for synthetic camouflaging skins. *Science* **358**(6360), 210–214 (2017). DOI 10.1126/science.aan5627. URL <https://science.sciencemag.org/content/358/6360/210> [3](#)
29. Renda, F., Giorelli, M., Calisti, M., Cianchetti, M., Laschi, C.: Dynamic model of a multi-bending soft robot arm driven by cables. *IEEE Transactions on Robotics* **30**(5), 1109–1122 (2014) [2](#)
30. Rivlin, R.S., Saunders, D.W.: Large Elastic Deformations of Isotropic Materials. VII. Experiments on the Deformation of Rubber. *Philosophical Transactions of the Royal Society A: Mathematical, Physical and Engineering Sciences* **243**(865), 251–288 (1950). DOI 10.1098/rsta.1951.0004 [8](#)
31. Rus, Daniela; Tolley, Michael T.: Design, Fabrication And Control Of Soft Robots. *Nature* pp. 467–475 (2015). DOI 10.1038/nature14543 [2](#)
32. Spivak, M.: A Comprehensive Introduction to Differential Geometry. Vol. V. Berkeley: Publish or Perish, Inc. XI (1979) [19](#)
33. Treloar, L.R.G.: The physics of rubber elasticity. Oxford University Press, USA (1975) [2](#), [8](#)
34. Trivedi, D., Lotfi, A., Rahn, C.D.: Geometrically Exact Models For Soft Robotic Manipulators. *IEEE Transactions on Robotics* **24**(4), 773–780 (2008) [2](#)
35. Trivedi, D., Rahn, C.D., Kier, M., Walker, I.D.: Soft Robotics : Biological Inspiration , State Of The Art , And Future Research **5**(3), 99–117 (2008). DOI 10.1080/11762320802557865 [1](#)
36. Truesdell, C., Noll, W.: The Non-Linear Field Theories of Mechanics. Springer (1965) [11](#), [20](#)
37. Walker, L.B., Harris, E., Pontius, U.: Center of gravity of human head and neck. In: ANATOMICAL RECORD, vol. 169, p. 448. WILEY-LISS DIV JOHN WILEY & SONS INC, 605 THIRD AVE, NEW YORK, NY 10158-0012 (1971) [5](#)
38. Walker, L.B., Harris, E.H., Pontius, U.R.: Mass, volume, center of mass, and mass moment of inertia of head and head and neck of human body. Tech. rep., SAE Technical Paper (1973) [5](#), [6](#)
39. Weisstein, E.W.: Barycentric coordinates (2003) [26](#)
40. Zambrano, D., Cianchetti, M., Laschi, C., Hauser, H., Füchslin, R., Pfeifer, R.: The Morphological Computation Principles As A New Paradigm For Robotic Design. Opinions and Outlooks on Morphological Computation pp. 214–225 (2014) [1](#)